

## The near-coastal microseism spectrum: Spatial and temporal wave climate relationships

Peter D. Bromirski

Integrative Oceanography Division, Scripps Institution of Oceanography, University of California, San Diego, La Jolla, California, USA

Fred K. Duennebieer

Department of Geology and Geophysics, University of Hawaii at Manoa, Honolulu, Hawaii, USA

Received 17 August 2000; revised 16 February 2001; accepted 20 August 2001; published 22 August 2002.

[1] Comparison of the ambient noise data recorded at near-coastal ocean bottom and inland seismic stations at the Oregon coast with both offshore and nearshore buoy data shows that the near-coastal microseism spectrum results primarily from nearshore gravity wave activity. Low double-frequency (DF), microseism energy is observed at near-coastal locations when seas nearby are calm, even when very energetic seas are present at buoys 500 km offshore. At wave periods  $>8$  s, shore reflection is the dominant source of opposing wave components for near-coastal DF microseism generation, with the variation of DF microseism levels poorly correlated with local wind speed. Near-coastal ocean bottom DF levels are consistently  $\sim 20$  dB higher than nearby DF levels on land, suggesting that Rayleigh/Stoneley waves with much of the mode energy propagating in the water column dominate the near-coastal ocean bottom microseism spectrum. Monitoring the southward propagation of swell from an extreme storm concentrated at the Oregon coast shows that near-coastal DF microseism levels are dominated by wave activity at the shoreline closest to the seismic station. Microseism attenuation estimates between on-land near-coastal stations and seismic stations  $\sim 150$  km inland indicate a zone of higher attenuation along the California coast between San Francisco and the Oregon border. *INDEX TERMS:* 3025 Marine Geology and Geophysics: Marine seismics (0935); 4599 Oceanography: Physical: General or miscellaneous; 7299 Seismology: General or miscellaneous; *KEYWORDS:* microseisms, wave climate, microseism source areas, Rayleigh wave attenuation, microseism propagation characteristics, ocean bottom seismometer

### 1. Introduction

[2] Wind-generated ocean gravity waves excite pressure fluctuations that couple energy into seismic waves at the ocean bottom, causing the gravity wave induced noise called microseisms. While numerous studies have described the characteristics of wave-generated noise (see *Webb* [1998] and *Orcutt et al.* [1993] for reviews), the variability of noise in the [0.04,0.20] Hz band has not been thoroughly investigated, primarily because of sparse long-term monitoring. Knowledge of the generation areas that provide principal contributions to noise levels in this band, as well as noise propagation characteristics, is important for identifying optimal ocean bottom monitoring sites. Identifying near-coastal microseism source area characteristics has important implications for the reconstruction [*Bromirski et al.*, 1999] and/or monitoring of the wave climate in locations where near-coastal seismic stations are, or have been, in existence and where continuous buoy deployment has not been done and/or buoy maintenance is problematical. The intent of this

study is to clarify the spatial and temporal relationship between the ocean gravity wave climate and microseism levels along coastlines, focusing primarily on microseisms at frequencies below 0.30 Hz. The near-coastal swell-induced microseism level variation can then be used to infer the range of variability of long-period noise at the seafloor.

[3] Primary or "single-frequency" microseisms, observed at the gravity wave frequencies, are generated only in shallow water and produce a comparatively low amplitude spectral peak in the [0.04,0.1] Hz band [*Haubrich and McCamy*, 1969]. Although not well understood, possible mechanisms for coupling ocean wave energy directly to the solid earth include the interaction of the ocean wave pressure signal with the sloping seafloor and/or the breaking of waves at the shoreline [*Hasselmann*, 1963]. Microseisms at double the ocean wave frequency result from nonlinear interaction of ocean gravity waves with opposing components, with the amplitude of "double-frequency" microseisms proportional to the product of the amplitudes of the opposing ocean wave components producing them [*Longuet-Higgins*, 1950]. Numerous researchers have studied the double-frequency (DF) microseism mechanism (see *Kibblewhite and Wu* [1991] for a review). In addition to

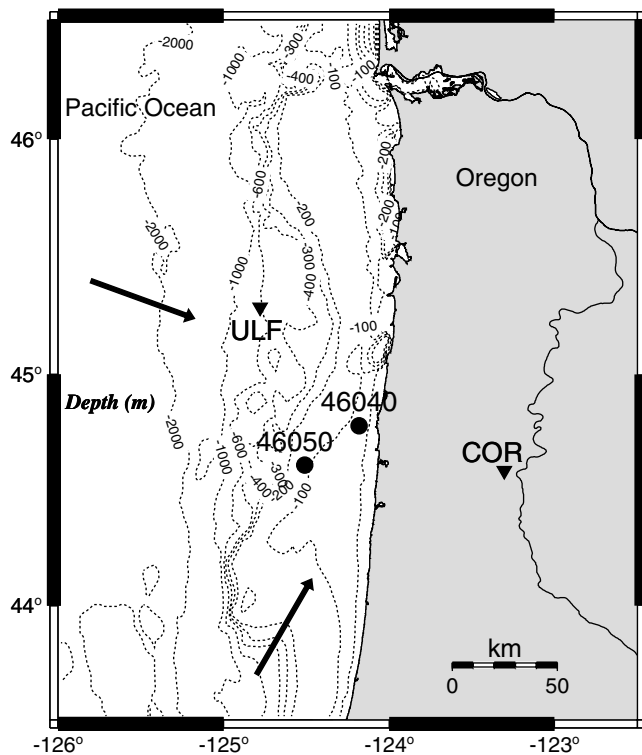


**Figure 1.** Locations of NOAA buoys (solid circles) and the ocean bottom, ULF, and inland, COR, seismometer sites (solid triangles) along the Oregon coast. Bathymetric contours are in meters below sea level, with the shallowest contour at 50 m. Arrows indicate approximate austral and boreal swell propagation directions.

multiple storm systems, opposing waves causing DF microseisms may occur near the wave generation region as the winds in a storm system vary in direction. Short-period DF microseisms can also be caused by rapid shifts in wind direction that generate opposing “local” seas [Kibblewhite and Evans, 1985; Herbers and Guza, 1994].

[4] Because the onset of microseisms associated with a particular wave event is generally emergent, the temporal variation of spectral levels is important to the identification of microseism source areas. Wave spectrum development and evolution characteristics are initially described, along with an overview of factors affecting microseism generation with a focus on concerns related to the shallow water near-coastal zone.

[5] The data presented in this study include ocean bottom pressure and seismometer data, buoy data, and land-based seismometer data collected during July 1991, and buoy and inland seismometer data from March 1999. During July 1991 the ULF/VLF Oregon '91 Experiment (ULF, ultralow frequency; VLF, very low frequency) was conducted ~65 km off the coast of Oregon at 45.3°N, 124.8°W in 600 m of water (ULF, Figure 1). The ULF/VLF system included buried CMG-3 Guralp broadband seismometers with a broadband hydrophone and a differential pressure gauge (DPG) on the seafloor. A detailed description of the experiment is given by Bromirski and Duennebier [1995]. The nearest operational buoy during the ULF experiment

was located at 44.8°, 124.3° (water depth of 112 m), ~20 km from the coast and ~60 km SSE of ULF, with deepwater buoy 46005 located ~500 km west of ULF (see Figure 15, below). Buoy data from July 1991 and March 1999 are available from the National Oceanic and Atmospheric Administration (NOAA) National Oceanic Data Center (NODC). A broadband near-coastal seismic station (COR) is located at Corvallis, Oregon, about the same distance inland as ULF is from the Oregon coast. Broadband seismometer data from COR were obtained from the Incorporated Research Institutions for Seismology Data Management Center (IRIS DMC).

[6] Using these data sets, the temporal relationships between the ocean gravity wave spectrum, the pressure levels at the ocean bottom, the microseism amplitude spectrum recorded by the buried ocean bottom seismometer, and the microseism spectrum recorded on land are established for the wave climate during the ULF/VLF experiment. Comparison of the temporal variation in wave energy at buoys 46005 and 46040 with microseism levels at ULF and COR allows estimation of the offshore contribution to the near-coastal microseism spectrum, as well as the determination of the transmission characteristics of microseism energy inland from near-coastal source areas.

[7] The observed relationships between the near-coastal gravity wave and microseism spectra during ULF/VLF are extended to most of the Oregon/California coast for storm events during March 1999. Broadband seismic data from the expanded Berkeley Digital Seismic Network (BDSN) (accessible through the Northern California Earthquake Data Center (NCEDC) [Romanowicz *et al.*, 1994]), in conjunction with NOAA buoys deployed along the West Coast (Figure 15, below), allow estimation of the magnitude of local near-coastal contributions to the microseism spectrum as swell from an extreme event focused along the Oregon coast propagates southward along the coast. The instruments at COR and BDSN stations are Streckeisen STS-1 and STS-2 broadband seismometers. Since gravity waves are dispersive, correlation of dispersion trends of ocean wave spectra from buoy measurements along the coast with concurrent nearby inland microseism spectral levels allows the differentiation of “telemicroseisms,” i.e., microseisms generated at distant locations and propagated as seismic surface waves, from microseisms generated by local wave activity. Localization of microseism source areas allows estimation of microseism attenuation between near-coastal and inland seismic stations.

## 2. Ocean Wave Microseism Spectrum

[8] Double-frequency microseism levels depend on the amplitudes of the interacting ocean wave spectral components, the size of the area of interaction, and the microseism propagation characteristics [Hasselmann, 1963]. While the dominant wave directional spectra can be estimated from buoy measurements, the opposing wave spectra and the area of interaction are generally uncertain. At periods of <10 s, the opposing wave field may contain contributions resulting from varying local winds and other relatively nearby storms. At longer periods, potential sources of opposing wave components, in addition to local seas, are distant storms and wave energy reflected from coastlines. Consequently,

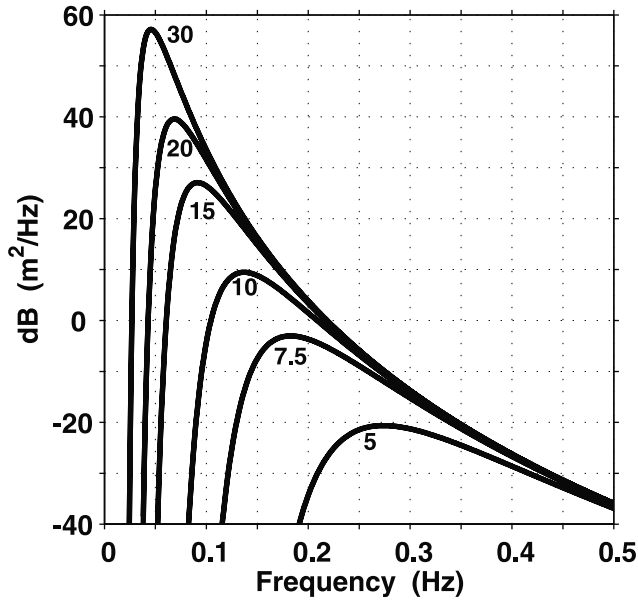


**Figure 2.** The Pierson-Moskowitz wave height spectrum for a fully developed sea under wind velocities of 5–30 m s<sup>-1</sup>. Typical wave periods for wave-wave interactions are between 3 and 20 s (0.2 and 0.05 Hz).

knowledge of the wave spectral characteristics and their distribution is essential to determination of the spatial and temporal variation of microseism levels.

### 2.1. Wind-Wave Relationships: Characteristic Spectral Patterns

[9] Storm winds generate dispersive gravity waves, with long-period waves traveling faster than short-period waves in deep water. The peak of the ocean wave spectrum for a fully developed sea depends on the duration of the maximum sustained wind speed of the storm and the fetch [Pierson and Moskowitz, 1964], where the fetch is the length of ocean acted on by the wind. Because the temporal variation in gravity wave spectral levels depends on storm size as well as the location of the monitoring site relative to the storm, the spectral pattern of wave energy associated with a single storm can potentially show three phases: onset, development, and either dissipation or dispersion. All storm phases from individual events are not always evident since a storm may form or dissipate over land and concurrent gravity wave arrivals from multiple storm systems at local, regional, and distant locations can obscure the spectral signatures. Changes in fetch size and orientation and in storm intensity as weather systems evolve can result in complicated spectral patterns.

[10] Locally generated “sea” is typically characterized by significant wave energy at periods of <10 s. As local seas develop, spectral levels are initially highest at short periods, demonstrated by the Pierson-Moskowitz wave model for several wind speeds (Figure 2). As the storm intensifies, the wave energy peak shifts to lower frequencies (longer periods), indicative of the progressive development of the in-fetch spectrum [Bretschneider, 1959].

[11] In contrast to local sea development the arrival of swell from distant storms shows the wave spectral peak

shifting from low to high frequencies as a result of the dispersion of ocean waves in deep water [Munk *et al.*, 1963]. Swell results when waves propagate out of the wave generation region. Swell with peak energy at very low frequencies is generated only by very high sustained wind speed over a large fetch. Very distant, large storms from the Southern Ocean produce narrowband swell arrivals [Munk *et al.*, 1963]. A conservative estimate of the maximum sustained wind speed (and relative size) of a storm can be obtained from the lowest gravity wave frequency (longest period) energy for the event.

[12] Gravity waves with angular frequency  $\omega$  and wave number  $k$  propagate according to the Airy dispersion relation

$$\omega^2 = gk \tanh(kh), \quad (1)$$

where  $h$  is the water depth and  $g$  is the gravitational acceleration. At locations sufficiently distant from the wave generation area for dispersion to be evident, the swell frequency displays a linear increase with time. Long-period, long-wavelength energy arrives first since ocean swell travels at the deepwater ( $kh \gg 1$ ) gravity wave group velocity,  $U_g$ , given by

$$U_g = \frac{1}{2} \left[ \frac{g}{k} \right]^{1/2}. \quad (2)$$

$U_g$  is  $\sim 30\%$  greater for 20-s waves (0.05 Hz) than for 15-s waves. An estimate of storm distance and wave origin time can thus be obtained from inversion of linearized dispersion trends using (2).

### 2.2. Factors Affecting Microseism Amplitudes

[13] The nonlinear interaction of opposing wave components having nearly the same wave number results in a pressure excitation spectrum that propagates away from the sea surface at twice the ocean wave frequency. Hasselmann [1963] showed that the double-frequency (DF) microseism excitation just below the free surface can be estimated from the gravity wave directional spectrum,  $W(\omega, \theta)$ , where  $\omega$  is the gravity wave angular frequency. The acoustic wave equation is used to propagate the pressure excitation spectrum to depth. Horizontal wave numbers,  $k$ , that are large compared to acoustic wave numbers result in evanescent DF pressure components that decay with depth  $h$  below the sea surface as  $e^{-k_z h}$  [Webb, 1992], where  $k_z$  is the vertical wave number. Figure 3 shows that the evanescent DF pressure components for  $k_z$  near the acoustic phase velocity,  $c$ , can be significant at the 600 m depth of the ULF sensors and in deeper water at low frequencies. Cox and Jacobs [1989] demonstrated the depth dependence of the DF pressure field from acoustic measurements near the ocean surface using a slowly profiling instrument. For horizontal wave numbers  $k < \omega/c$ , high phase velocity components of the pressure excitation spectrum propagate downward without appreciable attenuation. The nonresonant pressure spectrum for these components at nearly infinite depth is given by

$$P_\infty(\omega) = \frac{\pi \rho^2 g^2 \omega^3}{2c^2} \int_0^{2\pi} W(\omega/2, \theta) W(\omega/2, \theta + \pi) d\theta, \quad (3)$$

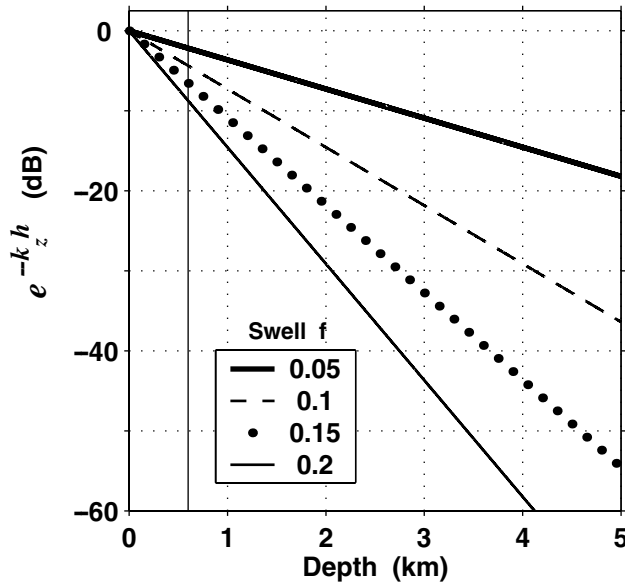


**Figure 3.** Decay of evanescent double-frequency excitation pressure with depth  $h$  below the sea surface for discrete vertical wave numbers  $k_z$  representing acoustic propagation for the associated gravity wave frequencies indicated. The curves were computed at  $2f$  and are referenced to  $h = 1$  m. The solid vertical line is at 600 m, the water depth above the ULF ocean bottom sensors.

where  $\rho$  is the density of seawater,  $g$  is the gravitational acceleration, and  $\theta$  is the gravity wave propagation direction [Webb and Cox, 1986]. At the seafloor, seismoacoustic waves are excited that propagate as Rayleigh waves or ocean acoustic modes. Interface waves can also be excited in deep water as a result of scattering from crustal irregularities [Kuperman and Schmidt, 1989; Schreiner and Dorman, 1990]. Energy reflected at or below the seafloor may force modes resonantly, significantly increasing DF microseism amplitudes at the ocean bottom [Webb, 1992]. The pressure-to-seismic transfer function that determines the partition of energy into these phases depends on the oceanic crustal structure and is proportional to the frequency [Hasselmann, 1963].

[14] The pressure excitation spectrum at the ocean bottom depends on the opposing wave components. In the open ocean the directional properties,  $I_q$ , of the wave spectrum can be modeled with a  $\cos^q(\theta)$  dependence, giving the wave-wave directional dependence,  $G(q)$ , as

$$G(q) = \int_0^{2\pi} I_q(\theta) I_q(\theta + \pi) d\theta \quad (4)$$

$$G(q) = \pi^{-\frac{1}{2}} 2^{-(q+1)} \frac{\Gamma(\frac{1}{2}q + 1)}{\Gamma[\frac{1}{2}(q + 1)]}, \quad (5)$$

where  $q$  is the beam parameter [Hughes, 1976]. The beam width is inversely proportional to  $q$ , with  $q = 0$  corresponding to an isotropic wave field. Then the pressure spectrum,  $S_P$ , at twice the wave frequency  $f$  can be written

in terms of the wave spectrum,  $S_w$ , as [Kibblewhite and Ewans, 1985]

$$S_P(2f) = \frac{2\pi^3 \rho^2 g^2}{c^2} f^3 S_w^2(f) G(q). \quad (6)$$

The sensitivity of  $S_P$  to beam width can be estimated using (6) by assuming  $S_w(f) = 1$  and then varying  $q$ . Figure 4 shows that the wave-wave interaction directional dependence ( $G(q)$ , dashed line) at  $G(5)$  is  $\sim 10\%$  of  $G(0)$ . The excitation pressure at the ocean bottom at a given wave frequency (Figure 4, solid lines) decreases by  $\sim 3$  dB per unit increase in  $q$  for  $q > 2$ . Also, for a given  $q$  and assuming the directional spectra are constant with frequency,  $S_P$  increases with wave frequency by 9 dB/octave. Consequently, the associated DF microseism spectrum will tend to be less peaked than the gravity wave source spectrum.

[15] Isotropic wave conditions are not expected nearshore for wave frequencies  $< 0.25$  Hz. However, if the dominant contribution to near-coastal DF levels results from near-shore wave-wave interactions of shore-reflected/scattered opposing waves from incoming swell, then an effective broad beam width may be appropriate and (6) may give a reasonable approximation of the excitation pressure at the ocean bottom.

[16] Crustal Rayleigh waves propagate with little attenuation through the ocean/seafloor waveguide [Dorman et al., 1991] and can potentially contribute to DF levels on the ocean bottom outside the generation area. Spatial and temporal variation of the opposing wave fields together with poorly known microseism propagation characteristics make the reliability of modeling DF microseism levels at the ocean bottom uncertain, although bounds on DF levels can be estimated by assuming wave directional spectrum and characteristic oceanic crustal structure models [Webb, 1992].

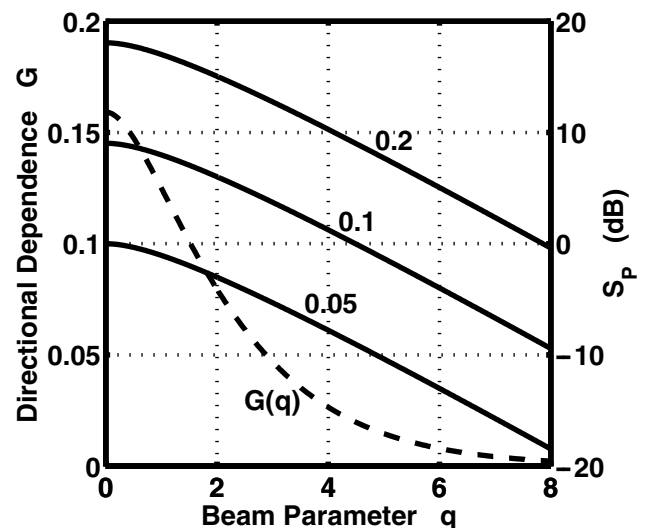


**Figure 4.** Excitation pressure at an infinite depth ocean bottom,  $S_P$  (solid lines), for wave frequencies  $f = 0.05, 0.1,$  and  $0.2$  Hz as a function of the beam parameter,  $q$ , with the associated directional dependence (dashed line).

[17] In the relatively shallow water near-coastal zone the ocean bottom is in the near field for the slowly propagating evanescent components of the pressure excitation spectrum. At 100 m depth the evanescent components provide much greater forcing compared with that observed in deepest water (Figure 3), exciting primarily interface waves that contribute significantly to the local ocean bottom noise spectrum [Schmidt and Kuperman, 1988]. Interface waves include Scholte waves that propagate along the water/sediment boundary and Stoneley waves that travel along deeper solid/solid boundaries at higher phase velocities and with less attenuation, with the propagation characteristics of both types of interface waves strongly dependent on the shear wave properties and thickness of the sediments [Schmidt, 1983]. Consequently, in addition to overhead forcing and DF energy propagating to ULF from nearby and distant open-ocean wave-wave interactions as Rayleigh waves, an additional interface wave contribution to the near-coastal DF microseism spectrum may originate in shallow near-shore waters.

### 2.3. Shallow Water Considerations

[18] The source area for primary microseism generation depends on the gravity wave wavelength and wave amplitude as well as the local bathymetry. Gravity waves begin to interact appreciably with the seafloor when the water depth,  $h$ , is less than half the deepwater wavelength,  $L_\infty$ , determined using the Airy linear wave theory approximation as  $L_\infty = gT^2/2\pi$ , where  $g$  is the gravitational acceleration and  $T$  is the wave period. Intermediate depths fall in the range  $1/20 < h/L_\infty < 1/4$ , where  $h < L_\infty/20$  is considered the shallow water zone. For 20-s waves,  $L_\infty \approx 600$  m, and for 8-s waves,  $L_\infty \approx 100$  m. The pressure at the ocean bottom from hydrodynamic forcing,  $P_b$ , relative to that near the sea surface,  $P_0$ , varies according to

$$P_b = \frac{P_0}{\cosh(kh)}, \quad (7)$$

where  $k$  is the wave number of the gravity wave. The hydrodynamic bottom pressure resulting from swell approaching the shore increases with both decreasing water depth and decreasing frequency. Figure 5 shows that  $P_b$  is strongly depth- and frequency-dependent and that the relative pressure at the ocean bottom decreases rapidly from  $\sim 35\%$  of the surface pressure at depths near  $L_\infty/4$  to  $\sim 8\%$  near  $L_\infty/2$ . This suggests that most primary microseism generation probably occurs at water depths less than the  $L_\infty/4$  bound. The bathymetry along the Oregon coast (see Figure 1) shows that the width of the intermediate depth region varies from  $\sim 50$  km for 20-s waves to  $\sim 5$  km for 8-s waves, indicating a significantly greater area for substantial bottom interaction for long-period swell.

### 3. Comparison of Gravity Wave Spectra With Ocean Bottom and Inland Microseism Spectra

[19] The general relationships between the wave climate and the microseism spectrum can be observed most clearly by comparing the temporal variation in spectral levels. The wave spectra presented in Figure 6 were obtained from buoy measurements taken for a 1024-s time period each hour and processed at the buoy to give wave spectral density esti-

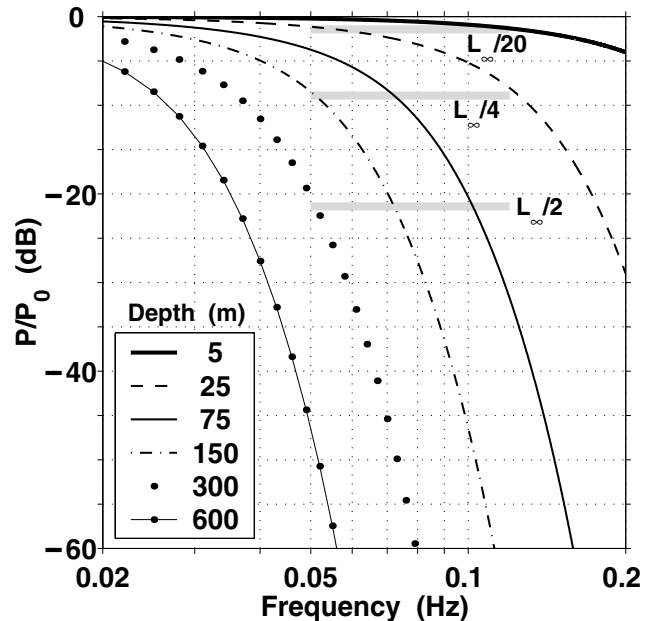


**Figure 5.** Pressure at the ocean floor,  $P_b$ , relative to the pressure near the sea surface,  $P_0$ , for the depths indicated. The horizontal gray bars show the relative pressure at depths  $h$  associated with the indicated fraction of the deepwater wavelength  $L_\infty$ .

mates having a resolution of 0.01 Hz with 28 equivalent degrees of freedom [Steele et al., 1985]. Pressure and seismometer data were processed following the Welch [1967] method of spectral averaging using three consecutive 512-s data segments with a Hanning taper and 256-s overlap. To reduce the variance in the spectral estimates, each spectral estimate (in dB) was averaged together with the two adjacent spectral estimates at both higher and lower frequencies. This procedure was repeated for sequential 256-s steps. The resulting power density spectral estimates are normalized to a 1-Hz bandwidth, with hourly averages obtained to correspond to the buoy sampling interval.

[20] Figures 6a and 6b show the wave spectral density estimates for offshore buoy 46005, located in over 4 km of water  $\sim 500$  km west of ULF, and nearshore buoy 46040, respectively (see Figures 1 and 15 for locations), during July 1991, when the ULF/VLF system was active. Associated wave climate parameters are shown in Figure 7. During the July 1991 ULF/VLF experiment, both local and more distant North Pacific storms were relatively small, resulting in low wave energy levels. The maximum significant wave height,  $H_s$  (the average height of the highest 1/3 of the waves), observed at buoy 46040 during 19–26 July was  $\sim 2$  m (Figure 7a), much lower than is typical during winter months. Most of the ocean wave energy is found in the [0.075, 0.20] Hz band (Figures 6a and 6b). The spectral levels are dominated by gravity waves from local and regional storm activity, as well as from larger storms near the Aleutian Islands and in the Gulf of Alaska. Wave energy at frequencies  $< 0.08$  Hz, at times other than the dominant boreal swell arrival during 23–24 July, results from low-amplitude, narrowband, long-period swell arrivals from more distant storms. The temporal variation in spectral

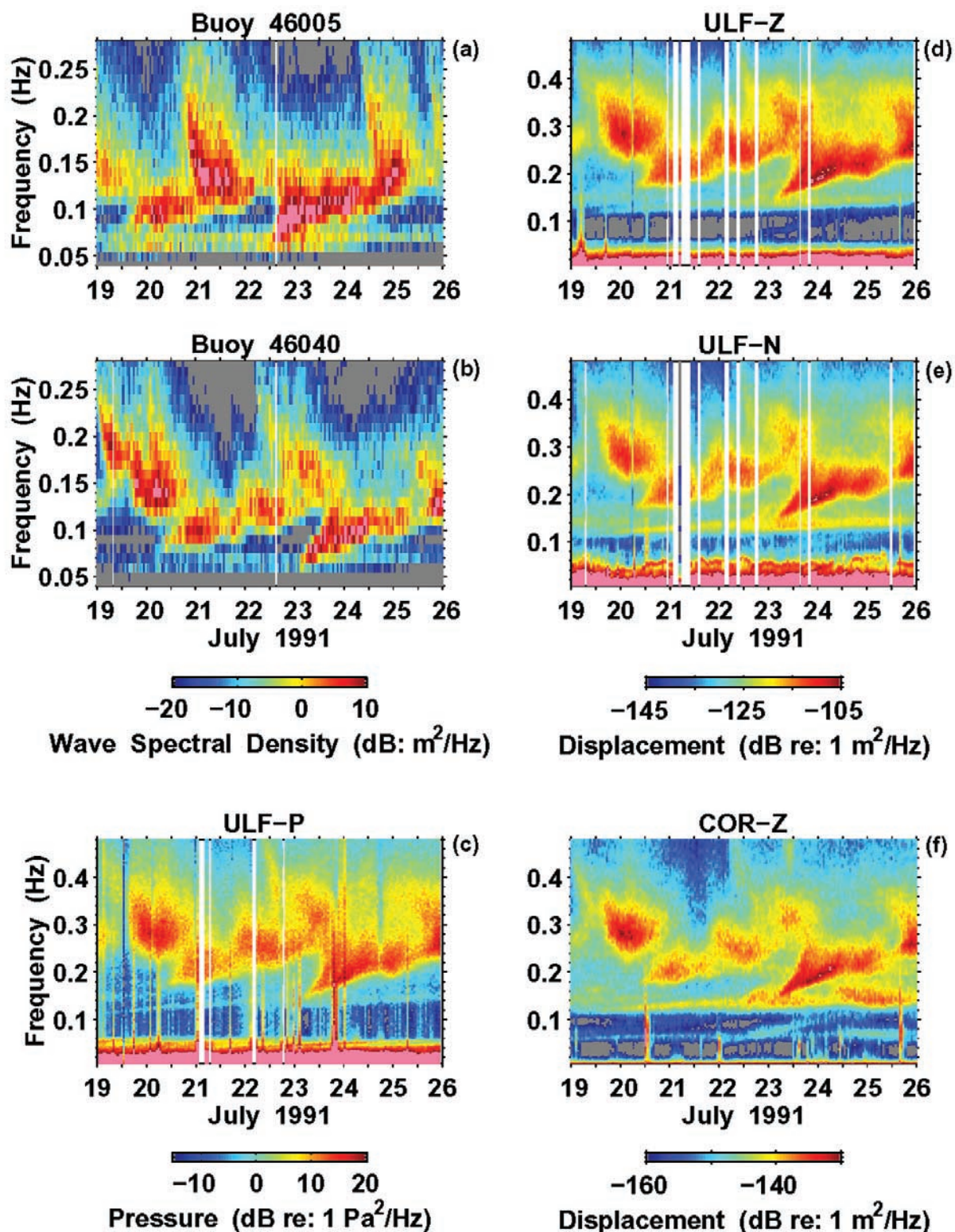


**Figure 6.** Wave spectral variation during the July 1991 ULF/VLF experiment at (a) offshore buoy 46005 and (b) nearshore buoy 46040. Ocean bottom power spectra at ULF from the (c) differential pressure gauge, ULF-P, (d) vertical seismometer, ULF-Z, and (e) northerly oriented horizontal component seismometer, ULF-N, for the same time periods as the wave data. (f) The corresponding displacement response at inland seismometer COR. All spectra are in dB, with spectral values outside the ranges shown set equal to their respective bound, with the highest amplitudes in pink. Figures 6a and 6b and Figures 6d and 6e have the same spectral ranges, respectively. Temporal tickmarks are at 12-hour intervals.

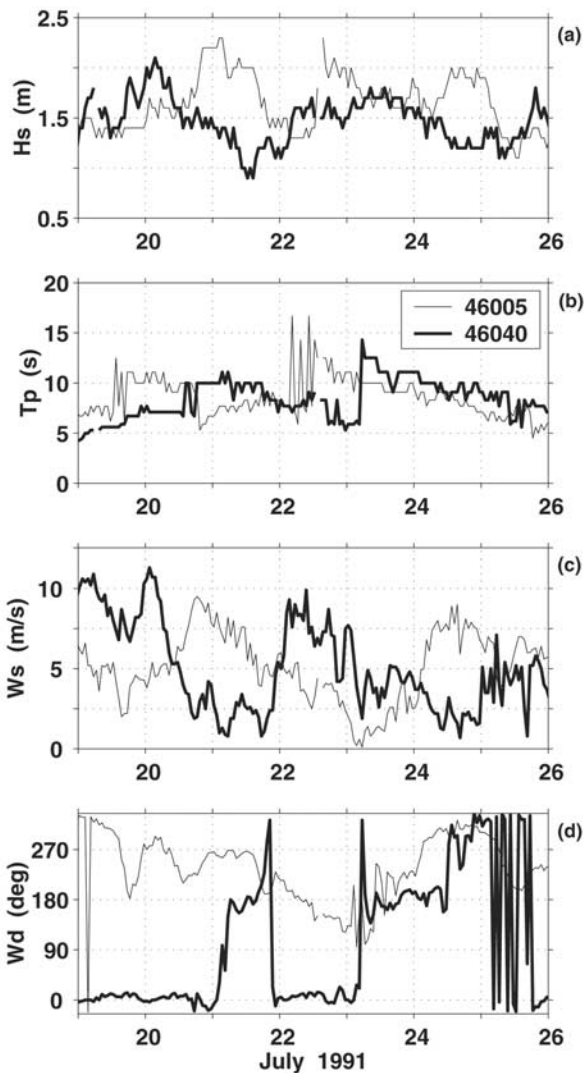


**Figure 7.** Wave climate parameters for buoy 46005 (thin line) and buoy 46040 (thick line) during the July 1991 ULF/VLF experiment off the Oregon coast: (a) significant wave height,  $H_s$ , (b) peak wave period,  $T_p$ , (c) wind speed,  $W_s$ , and (d) wind azimuth,  $W_d$ .

levels at buoy 46005 is similar to the near-coastal pattern at buoy 46040. However, since North Pacific storm tracks are generally west of buoy 46005, in most cases, wave energy arrives at buoy 46005  $\sim 12$ – $20$  hours before arriving at buoy 46040, depending on wave direction and storm and gravity wave group velocity ( $U_g$ , equation (2)) and consistent with the travel time at  $\bar{U}_g$  for the dominant wave frequencies. Comparison of the temporal wave spectral energy variation for the swell event on 23–24 July (Figures 6a and 6b) shows the delay between buoys 46005 and 46040.

[21] The variations in noise levels during one week of the ULF/VLF experiment from data recorded by the node 2 DPG (ULF-P), the Guralp vertical (ULF-Z), and the north-south horizontal (ULF-N) seismometers are shown in Figures 6c, 6d, and 6e, respectively. The pattern of spectral variation at frequencies above 0.10 Hz is very similar at all

ULF sensors and inland station COR (Figure 6f), with the different amplitude ranges for ULF-Z and COR-Z chosen to emphasize the similarity. Comparison spectra are given below. Spectral levels above 0.10 Hz are generally  $>15$  dB lower at COR-Z than at ULF-Z. Higher spectral levels at frequencies less than  $\sim 0.15$  Hz are observed at ULF-N compared with ULF-Z. Ultralong-period infragravity waves (at frequencies generally  $<0.05$  Hz), probably resulting from nonlinear interactions of refractively trapped long-period wave energy along shorelines [Guza and Thornton, 1982], are also observed by ocean bottom and near-coastal seismometers. The irregular band of energy at ULF-N near 0.05 Hz, adjacent to high infragravity wave levels at frequencies  $<0.03$  Hz, is unidentified noise. The narrowband primary microseisms observed at COR-Z near 0.06 Hz are masked at ULF-Z by high infragravity wave levels. Microseisms from dispersed swell arrivals will be discussed in section 3.3.

[22] Close similarity in energy concentration between the near-coastal wave and seismic spectra is observed, with the seismic microseism levels at twice the ocean wave frequencies correlating with corresponding wave energy. The highest wave energy levels at buoy 46040 have nearly a one-to-one correspondence with the highest microseism levels at both ULF and COR. Simultaneous wave arrivals can be differentiated in the seismic data by their frequency content. Local seas generated by local winds dominate the high-frequency components, while swell from distant storms is observed as dispersed low-frequency components. Observation of this dispersion in the microseism spectrum implies that the swell has traveled a significant distance before generating the observed microseism energy. Comparing the pressure and seismometer spectra (Figures 6c–6f) shows that other than the first half of 19 July, the near-coastal DF microseism levels are directly related to the local pressure excitation spectrum resulting from nearby wave-wave interactions. Nearly all of the observed temporal variation of associated DF spectral levels can be explained by local wind wave and swell activity, as opposed to energy arriving as seismic Rayleigh waves generated beneath distant storms. Such energy would not show the observed dispersion trends but would reflect the evolution of the storm at its source.

### 3.1. Comparative Spectra

[23] Local storm intensity can be characterized by the wind speed,  $W_s$ , levels. Relatively small, local storms typically generate peak wave periods,  $T_p$ , of  $<10$  s. The strongest local event during the ULF/VLF experiment occurred on 19–20 July, with relatively abrupt changes in wind speed observed with the passage of the storm (Figure 7). The characteristic pattern associated with local sea development and dissipation is evident for both the wave energy and ocean bottom pressure data from 19 July, 1200 UT to 20 July, 1200 UT period (Figures 6b and 6c).

[24] DF microseism generation from swell arrivals generally does not depend strongly on local wind conditions. The peak spectra for the 20 July (Figures 8a, 8b, and 8c) and 23 July (Figures 8d, 8e, and 8f) events show spectral peaks for the ocean bottom pressure and displacement at nearly double that of the wave spectrum at nearshore buoy 46040. Primary microseisms for the 20 July short-period event are masked by the small DF microseism peak near 0.13 Hz that results from the narrowband swell arrivals observed at

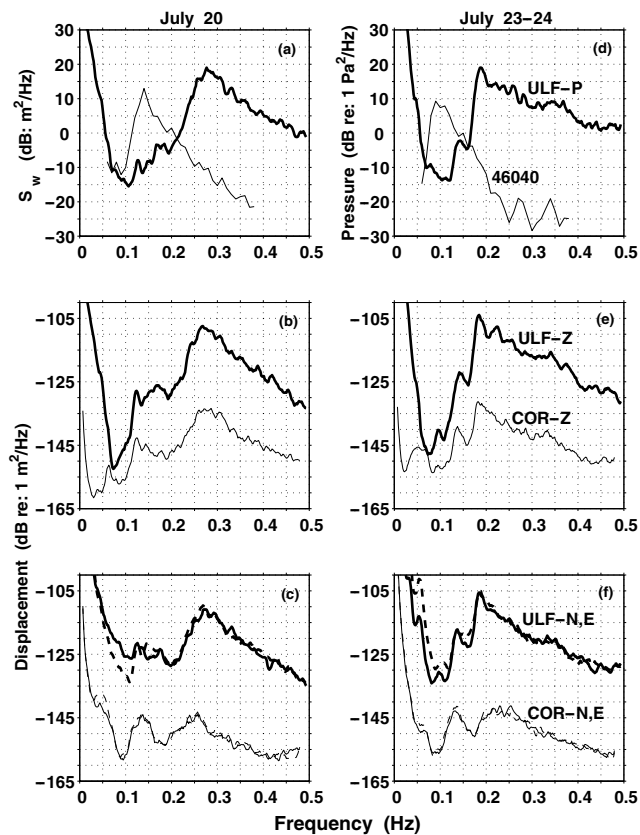


**Figure 8.** Peak spectra associated with wave events along the Oregon coast during 20 July (Figures 8a–8c) and 23–24 July 1991 (Figures 8d–8f). (a) and (d) Ocean bottom pressure peak power spectra, ULF-P (thick lines) and wave spectral density estimates (thin lines),  $S_w$ , for the same time periods. (Vertical axis labels in Figures 8a and 8d apply to both Figures.) (b) and (e) The vertical displacement peak power spectra for the two events. (c) and (f) Orthogonal horizontal displacement power spectra at ULF and COR for the same time periods. (Labels shown in Figures 8d–8f correspond to similar line types in Figures 8a–8c).

buoys 46005 and 46040 in the [0.06,0.08] Hz band. The Pierson-Moskowitz wave spectrum (Figure 2) for  $W_s = 10$  m/s corresponds well with the wave spectrum for the peak of the 20 July event both in frequency and amplitude (Figure 8a), while that is not the case for the 23 July swell event where the local  $W_s$  is not associated with the long-period swell spectral components.

[25] The DF microseism levels from boreal swell are  $\sim 25$  dB higher at ULF than at COR at the dominant DF peaks for the vertical sensors and  $\sim 35$  dB higher at ULF for the horizontal sensors. In contrast, differences in spectral levels between ULF and COR for the austral swell-induced DF microseism peaks near 0.13 Hz (Figure 8) are  $\sim 15$  dB and  $\sim 25$  dB for the vertical and horizontal sensors, respectively. The smaller difference for the 0.13-Hz DF peaks may result because nearshore generation dominates DF levels at ULF for the long-period swell, while DF levels for the shorter-period waves include some DF energy from overhead as well as nearshore wave-wave interaction. Although some telemicroseism energy is probably included in these micro-

seism levels, comparison of the microseism spectral variation during 18–25 July from seismic stations BRIB and JRSC (not shown) in the San Francisco region (see Figure 15, below, for locations) with that from COR indicates that most of the microseism energy at COR resulting from the austral arrivals is generated along the Oregon coast.

### 3.2. Correlation Between Ocean Wave and Microseism Spectra

[26] Comparison of wave and microseism spectrum levels in Figure 6 shows that the near-coastal microseism spectrum is highly correlated with the near-coastal wave climate measured at buoy 46040. The relationships between buoy 46040 ULF and COR displacements can be quantified by cross-correlating  $H_s$  determined for both seismic and wave data from  $H_s = 4m_0^{1/2}$ , where  $m_0$ , the band-limited zeroth moment of the spectrum,  $S(f)$ , is obtained as  $m_0 = \int_{f_1}^{f_2} S(f) df$ , with the integration limits,  $[f_1, f_2]$ , for the seismic data of [0.11,0.48] Hz double the gravity wave [0.055,0.24] Hz band. Spectral averages of 30 min duration for the seismic data shown in Figure 6 were used to obtain the band-limited  $H_s$  (Figure 9), with all  $H_s$  data low-pass filtered to remove data glitches and other noise.

[27] In general, elevated wave  $H_s$  at buoy 46040 (Figure 9a) is associated with elevated pressure and seismic  $H_s$  at ULF and COR. Figure 10a shows the correlation coefficient,  $R^2$ , as a function of lag for the vertical seismometer, ULF-Z, and the ocean bottom pressure, ULF-P, with the wave height at buoy 46040 and with each other. Figure 10b shows  $R^2$  between the inland vertical seismometer, COR-Z, and each of the components in Figure 10a with a positive lag, indicating that COR-Z leads the associated component. Component lags in Figure 10a are similarly related. Figure 10 confirms that the energy in the DF microseism band at buoy 46040, ULF, and COR is generally well correlated. As expected, the colocated ULF-Z and ULF-P show good correlation. Both ULF-Z and ULF-P tend to lag  $H_s$  at buoy 46040, with a similar lag observed between ULF-Z and ULF-P. Correlation between ULF-P and buoy 46040 is much better than ULF-Z-buoy 46040, most likely because the pressure sensor on the ocean floor is less sensitive to interface wave modes than is ULF-Z buried in the sediments.

[28] Surprisingly good correlation is observed between COR-Z, located  $\sim 60$  km inland (see Figure 1), and the near-coastal gravity wave and ocean bottom band-limited  $H_s$  levels (Figure 10b). The COR-Z-buoy 46040 correlation function is nearly symmetric about zero lag, consistent with the dominant DF source area located at the coastline nearest COR. The correlation between COR-Z and buoy 46040 is much better than ULF-Z-buoy 46040, probably resulting from low phase velocity Rayleigh/Stoneley wave DF energy observed at ULF [Schmidt and Kuperman, 1988] (decreasing the ULF-Z-buoy 46040 coherence) that does not propagate inland. The correlation between COR-Z and ULF-P is very similar to ULF-Z-ULF-P, but with COR having a bias toward leading ULF. In the absence of locally generated seismoacoustic energy as at ULF, telemicroseisms from nonlocal coastal locations will provide a greater percentage of the DF energy at COR, causing the slight bias of COR leading ULF. The  $R^2$  function between COR-Z and ULF-Z shows a somewhat broader and flatter peak than COR-Z-buoy 46040, with ULF-Z tending to lag COR-Z, consistent

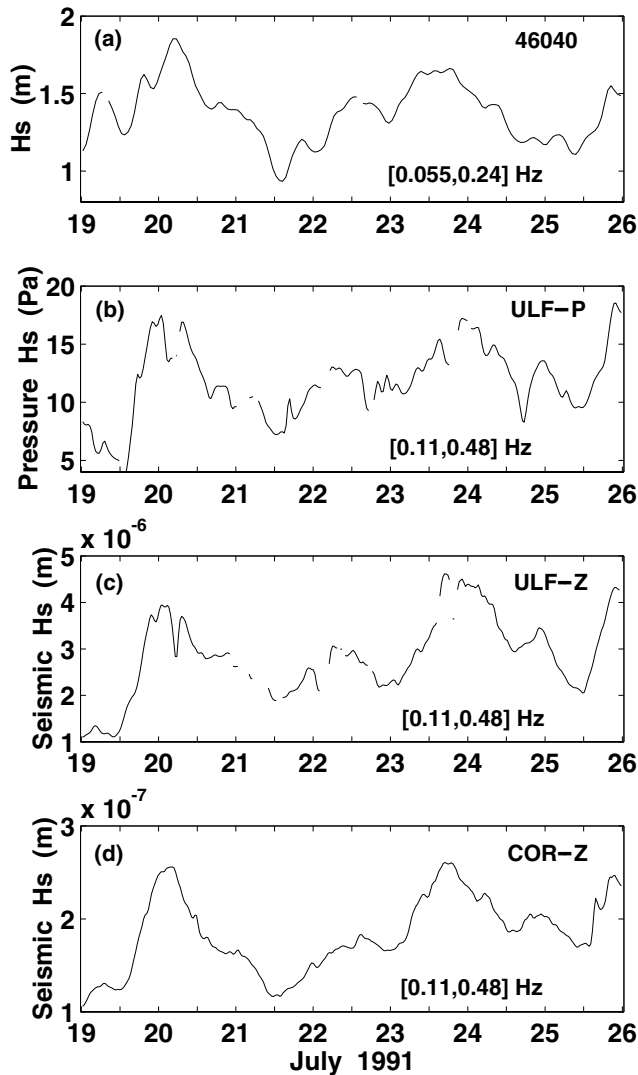


**Figure 9.** (a) Band-limited significant wave height,  $H_s$ , determined from wave spectra measured at buoy 46040 during the ULF/VLF experiment. (b), (c), and (d) Corresponding  $H_s$  determined for the ocean bottom pressure, ULF-P, and vertical seismometer, ULF-Z, and the inland seismometer, COR-Z, respectively. Respective integration bands are indicated.

with DF levels resulting from a distributed local nearshore source area to the north and south of COR.

[29] Some of the apparent differences between the wave spectrum and associated DF microseism variation can be attributed to local wave climate variability. Buoy 46050 was initially deployed in September 1991, ~25 km north of buoy 46040 (see Figure 1). During 9–16 January 1992 (when both buoys were operational), long-period swell with  $H_s > 5$  m reached the Oregon coast. Cross correlation of band-limited  $H_s$  between buoys 46050 and 46040 shows that  $H_s$  in the [0.055, 0.24] Hz band is well correlated, as indicated by the high  $R^2$  (Figure 10b, dashed line). However,  $H_s$  is observed to vary locally by as much as 25% and accounts for part of the variation observed for the wave spectral patterns and  $R^2$  functions between buoy 46040 and those at ULF-Z and COR-Z, assuming that the generation

area that provides the dominant contribution to the local microseism spectrum is at least as large as the separation between buoys 46040 and 46050. Correlation between COR-Z and buoy 46040 for January 1992 (Figure 10b, dotted line) gives an  $R^2$  function that is somewhat less than the buoy 46050 and buoy 46040 difference for the same time period. The COR-Z-buoy 46040 correlation is biased toward COR-Z leading. The relatively high  $R^2$  of COR-Z-buoy 46040 at longer leads than during July 1991 suggests that DF levels at COR during January 1992 include some DF energy generated by higher wave energy observed at

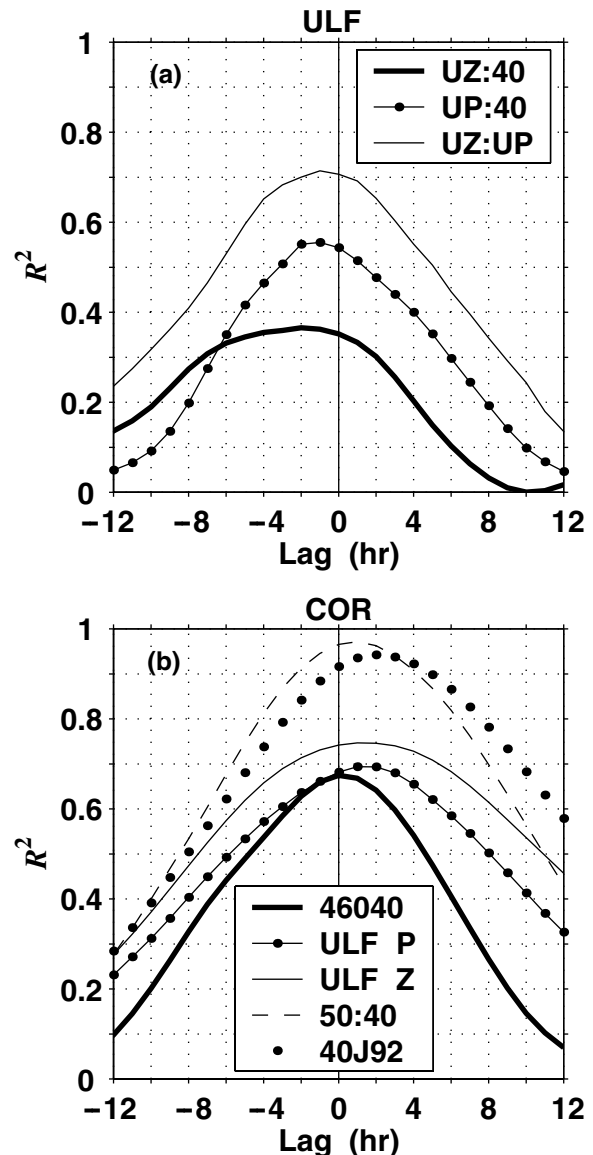


**Figure 10.** (a) Correlation coefficient,  $R^2$ , as a function of lag between band-limited  $H_s$  (Figure 9) for ULF-Z and buoy 46040, UZ:40, ULF-P and buoy 46040, UP:40, and ULF-Z and ULF-P, UZ:UP. (b)  $R^2$  as a function of lag between COR-Z and buoy 46040, ULF-P, and ULF-Z, respectively. Also included in Figure 9b are correlations between buoys 46050 and 46040 (50:40) and between COR and buoy 46040 (40J92) for January 1992 (see legends). A positive lag implies the first component leads.

near-coastal buoys along the coast to the north of buoy 46050 prior to the wave energy arriving locally.

[30] All observed correlations are consistent with the dominant contribution to the near-coastal DF microseism spectrum coming from relatively local, nearshore wave-wave interactions. Figures 10a and 10b show a consistent relationship; that is, the ocean bottom sensors at ULF tend to lag both buoy 46040 and COR. For the low sea states dominated by gravity waves propagating from the west, the variation of DF levels at COR is nearly concurrent with associated wave energy at buoy 46040, i.e., the nearest coastline. Although the variable DF source area and propagation effects make the temporal resolution of the inherently emergent microseism signal onset uncertain, these correlations suggest that the dominant local DF generation area is both closer to shore and closer to COR than it is to ULF.

### 3.3. Dispersed Swell Arrivals

[31] Long-period dispersion trends recorded in shallow water are more clearly characterized using ground acceleration response spectra (Figure 11), where infragravity wave spectral levels that mask these signals are less dominant than in displacement spectra (Figure 6). The seismometer data were processed using 1024-s segments with 512-s overlap and then obtaining successive 30-min averages. The number of degrees of freedom is small to preserve the resolution of these nonstationary arrivals. The low-frequency portion of the resulting power density spectra for the ULF-Z data is shown in Figure 11a. Transients on 19 July are shots used for instrument localization. Earthquake surface wave arrivals ( $M_b \geq 5$ ) are observed on 20 July, 1200 UT (Figures 11b and 11c, discussed below) and on 25 July, 1800 UT. Other transients are small local earthquakes or missing data.

#### 3.3.1. Boreal swell arrivals

[32] During the period of time shown in Figure 11a, wave energy from two boreal storms was arriving at ULF. A relatively small storm south of the Aleutian Islands traveled eastward toward the Oregon coast between 12 July and 15 July. Low-amplitude swell energy in the [0.08,0.12] Hz band from this storm arrives at buoy 46040 between 20 July, 1200 UT, and 21 July, 1200 UT (Figure 6b), with associated DF microseisms observed at frequencies in the [0.16,0.24] Hz band during that time period (Figure 11a). The lag between the arrival of wave energy from the more intense swell during 23 and 24 July at buoys 46005 and 46040 (Figures 6a and 6b) suggests that these waves also originated in the North Pacific. Single-frequency microseisms, bounded by dashed lines d and e in Figure 11a, are observed during 23 and 24 July when the peak wave energy reaches the Oregon coast. The double-frequency microseisms resulting from these waves, bounded by lines f and g, dominate the microseism spectrum from 23 to 24 July. Estimated dispersion trends beginning on 23 July, 0800 UT, for waves generated at the end of the storm correspond to lines e and g, while lines d and f are associated with dispersed wave arrivals generated near the beginning of the storm. Since trends e and g indicate some dispersion, the storm either dissipated at sea or made landfall distant from ULF. Inversion of the dispersion trends using equation (2), assuming a mean water depth of 4500 m, gives distances

and origin times of  $\sim 3500$  km and  $\sim 700$  km on 19 July, 0400 UT, and 22 July, 1100 UT, for waves at the beginning and end of the storm, respectively. These distances place the storm in the Gulf of Alaska, consistent with buoy data from that region. Note that the increase in infragravity wave spectral levels near 0.025 Hz peak on about 23 July, 1600 UT, concurrent with the arrival of this swell.

#### 3.3.2. Austral swell arrivals

[33] The linear narrowband dispersion trends observed at ULF in the [0.04,0.06] Hz band (dashed lines a, b, and c, Figure 11a) are characteristic of gravity waves from very distant, large storms. Note that these trends are at slightly lower frequencies and hence are different from the primary microseisms observed in Figure 6f at COR. Also note that buoys 46005 and 46040 detect austral swell arrivals near 15 s (0.07 Hz, Figures 6a and 6b) but the narrowband, lower-amplitude arrivals at frequencies  $< 0.06$  Hz are not clearly observed, possibly related to the buoy processing methodology. Inversion of the dispersion trends in Figure 11a indicates that storm systems occurred at distances of  $\sim 10,000$  km and  $18,000$  km, with trend c caused by swell from the most distant event as indicated by its shallower slope. These distances from the Oregon coast place the location of the swell-generating storms in the extreme South Pacific and Southern Oceans. Weather charts from 5 to 15 July 1991 were obtained from the Bureau of Meteorology, Melbourne Royal Military College, to search for suspect storm systems. The charts show that persistent mesoscale convective cells developed over the South Pacific and Southern Oceans between 5 and 14 July. The Southern Ocean storm, associated with trend c, produced a very large fetch on the order of 1000–2000 km near ( $100^\circ\text{E}$ ,  $55^\circ\text{S}$ ), capable of generating 25-s waves. The South Pacific storm, trend b, was smaller in areal extent but developed very strong barometric pressure gradients, reaching maximum intensity while located near ( $145^\circ\text{W}$ ,  $60^\circ\text{S}$ ) on 11 July 1991. The apparent fetch of these storm systems was aligned to direct wave energy toward the Oregon coast. *Munk et al.* [1963] identified narrowband swell arrivals from high-latitude Southern Hemisphere storms that travel through the “Tasman Sea window,” similar to those producing trend c, with the narrowness of spectral band the result of wave front spreading and “island filtering.” The reasonably good agreement of the dispersion trend c inversion for both the time and distance of the austral storms suggests that these signals were generated locally.

### 3.4. Earthquake Surface Wave Arrivals

[34] During the ULF/VLF experiment, several teleseismic earthquake surface wave arrivals were recorded. The largest magnitude event  $m_b = 5.5$  occurred on 20 July 1991, 1148:47 UT, was located in the Aleutian Islands near  $54.9^\circ\text{N}$ ,  $161.5^\circ\text{W}$  at 35 km depth. The data were processed using 1024-s segments with a Hanning window and 32-s overlap and no additional averaging. The vertical component spectral levels for this event at ULF and COR (Figures 11b and 11c, respectively) have similar amplitudes for the fundamental Rayleigh mode in the [0.04,0.08] Hz band, identified at ULF (Figure 11b) by the propagation time curve (white line) computed using equation 4.154 of *Ewing et al.* [1957] for a 4.5-km water layer over a half-space crustal model with  $\rho_1 = 1.03$  g/cm<sup>3</sup>,  $\rho_2 = 3.1$  g/cm<sup>3</sup>,

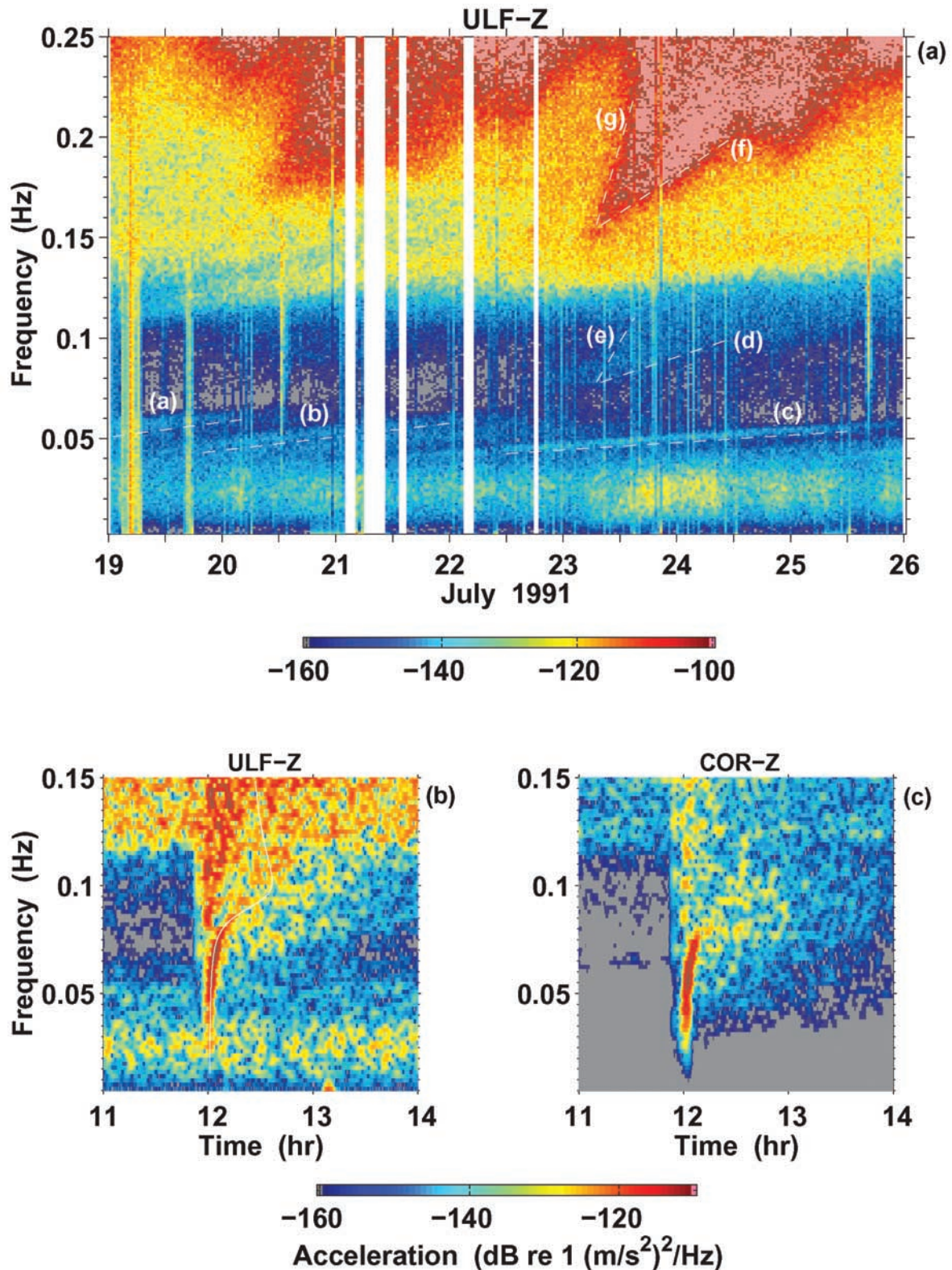


**Figure 11.** (a) Vertical component acceleration response spectral variation at ULF, with locally generated primary microseisms resulting from dispersed swell arrivals indicated by dashed lines a–e. Dashed lines g and f bound double-frequency microseisms associated with lines d and e. (b) Earthquake surface wave arrivals on 20 July, 1200 UT, at ULF-Z. (c) Surface wave arrivals from the same earthquake at COR-Z. Power spectral values outside the ranges shown are set equal to their respective bound.

$\alpha_1 = 1.503$  km/s,  $\alpha_2 = 7.35$  km/s,  $\beta_2 = \alpha_2/\sqrt{3}$ , and  $c_R = 0.9195\beta_2$ . The reasonably good fit using this crude two-layer model suggests that these arrivals are dominated by energy propagating through the oceanic crust, consistent with the great circle path from the epicenter to ULF and COR. Similar spectral levels in the [0.07,0.15] Hz band at ULF and COR indicate that fundamental mode Rayleigh waves are not appreciably attenuated during transmission inland from the continental shelf. Thus large differences in DF levels between ULF and COR are not due to differences in Rayleigh wave energy, with the much higher DF levels at ULF probably resulting from interface wave energy that does not propagate inland.

**3.5. Wave Climate Variation: Source Area Implications**

[35] Wave climate comparisons between offshore and nearshore buoys are useful to estimate the location of the principal source area for the dominant contribution to the DF microseism spectrum. In addition to localizing the microseism source area the importance of varying wind speed,  $W_s$ , and wind direction,  $W_d$ , in providing opposing wave components for DF microseism generation can also be estimated from concurrent nearby wave climate and seismometer data.

[36] Comparison of Figure 6a with Figures 6b–6f suggests that little DF microseism energy from the open ocean reaches the coast. For example, during occurrences of the highest wave energy at buoy 46005 during 21 July, 0400–1800 UT, and 22 July, 1200–2400 UT, low energy is observed at buoy 46040 and for associated DF levels at both ULF and COR during the same time periods. However, the low-energy wave climate during the ULF/VLF experiment must be considered. To investigate the coastal Oregon microseism spectrum under more energetic wave conditions, the nearshore wave spectrum and microseism spectrum at COR are compared for an extreme storm/swell event with significantly higher wave energy offshore. Figure 12 shows the temporal variation in wave spectral density,  $S_w$ , between offshore buoy 46005 and nearshore buoy 46050 and microseism levels at COR during 18 March 1999 (see Figures 1 and 15, below, for locations). The band-limited significant wave height,  $H_s$ , was obtained for the gravity wave spectral density estimates from buoys 46005 and 46050 in the [0.045,0.125] Hz band (Figure 13a) and for corresponding seismometer data from COR. Figure 13 shows that the peak  $H_s$  at nearshore buoy 46050 trails the  $H_s$  peak at buoy 46005 by ~14 hours, consistent with the travel time for  $U_g$  of ~36 km/h from equation (2) for the dominant 14-s gravity waves from the northwest in the vicinity of buoy 46005. The spectral energy variation at COR (Figure 12c) closely follows the wave spectral density pattern at nearshore buoy 46050 (Figure 12b), consistent with the relationships observed during the ULF/VLF experiment. The highest microseism levels observed on land occur only when waves from this storm reach the coast.

[37] Differences in spectral patterns between buoy 46050 and COR-Z near the arrival of the wave spectrum peak at buoy 46005 (Figure 12) suggest that some DF microseism energy in the [0.12,0.2] Hz band detected at COR propagates as Rayleigh waves from the vicinity of buoy 46005. Assuming that similar near-coastal wave energy levels will

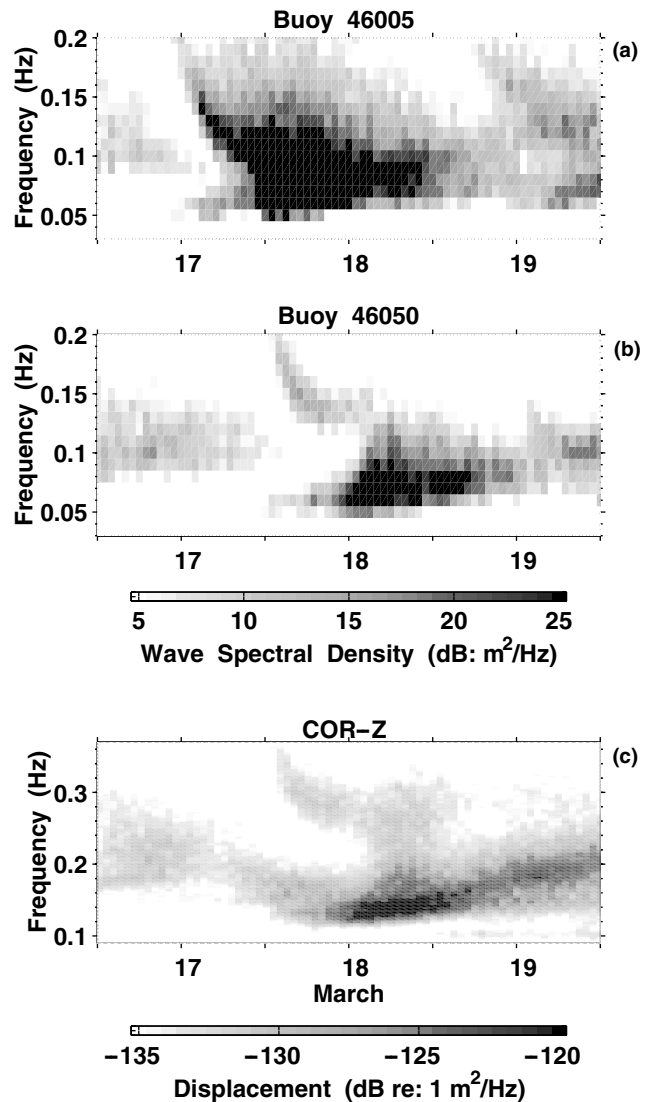


**Figure 12.** Wave spectra at (a) offshore buoy 46005 and (b) nearshore buoy 46050 during 18 March 1999. (c) Associated DF microseism power spectral levels at seismic station COR.

produce similar microseism levels at COR, comparison of spectral levels at buoy 46050 (Figure 12) with similar wave energy spectral levels at buoy 46040 during the ULF/VLF experiment (Figure 8) suggests that from 5 to 10 dB of the DF energy on 17 March, 1330 UT, at COR originates from nonlocal wave-wave interactions. Some of this energy most likely results from DF microseisms generated at other coastal locations. Increased seismic  $H_s$  at COR for the long-period DF band (Figure 13a, thin solid line) both before and after the arrival of the swell peak at buoy 46050 can be attributed to near-coastal DF generation to the north (on 17 March) and to the south (on 19 March) of COR. Hence relatively little DF energy generated offshore may reach COR. The telemicroseism contribution from nonlocal near-coastal locations will be discussed in section 4. Although not shown, similar relationships between offshore and nearshore buoys for other storm events and local near-coastal microseism levels along the Oregon coast are

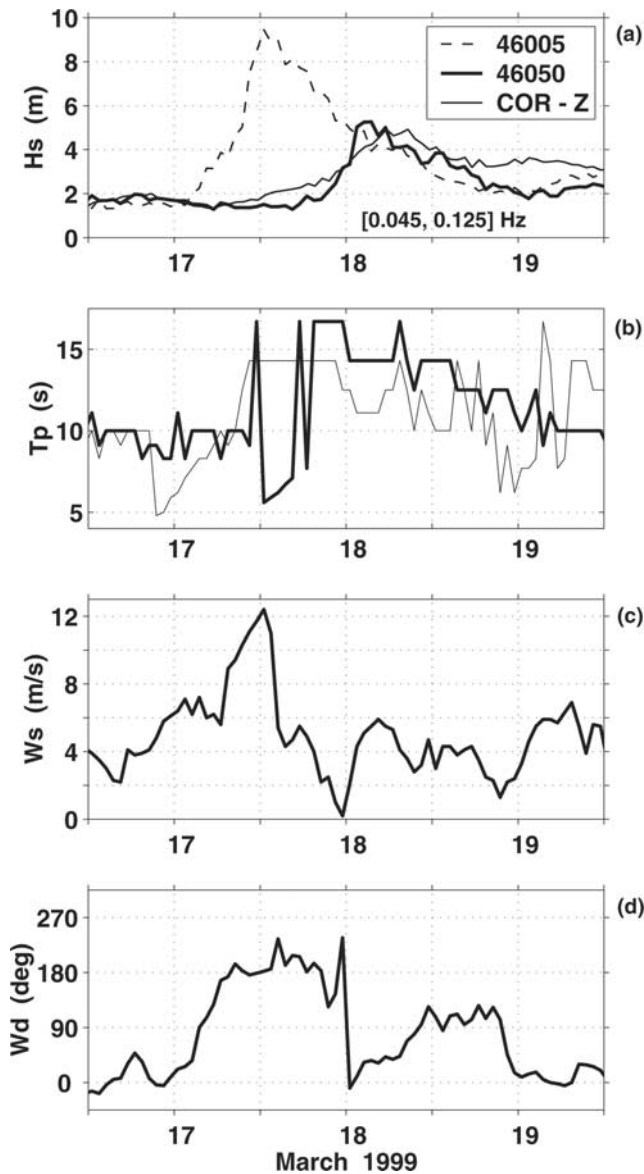


**Figure 13.** Wave climate parameters for buoy 46005 (dashed line) and buoy 46050 (thick line) off the Oregon coast during March 1999: (a) Band-limited significant wave height,  $H_s$ , for the frequency band shown, (b) peak wave period,  $T_p$ , (c) wind speed,  $W_s$ , and (d) wind azimuth,  $W_d$ , plotted from  $-45^\circ$  to  $315^\circ$ . The seismic  $H_s$  at COR in Figure 13a, obtained at double the band limits shown, is scaled by its mean for comparison.  $W_s$  and  $W_d$  are unavailable from buoy 46005 for this event.

also observed along the California coast between buoys 46002 and 46027 and seismic station YBH, buoys 46002 and 46022 and seismic station ARC, buoys 46059 and 46013 and seismic station BRIB, and buoys 46059 and 46042 and seismic station SAO (see Figure 15, below, for locations).

[38] The seismic levels at COR for the 18 March 1999 event (Figure 14, solid line) clearly shows primary and DF microseism peaks at the swell and double frequencies, i.e., at 0.07 and 0.14 Hz, respectively. Although the wave energy

for the 18 March 1999 event is nearly 25 dB above that for the 20 July 1991 event (Figure 14), the DF peak at COR is only slightly more than 10 dB higher. A possible explanation is that the longer-period, high-amplitude wave components undergo significantly more dissipation, resulting in reduced opposing components from shore reflection. *Forristall and Reece* [1985] observed more than a 50% reduction in wave energy for an extreme event in the Mississippi Delta between deep and shallow water platforms separated by 30 km, a distance similar to that of buoy 46050 from the shore, demonstrating that significant dissipation losses are possible. *Bouws and Komen* [1983] found dissipation to be an important factor in limiting wave height for a severe storm in North Sea water depths near 35 m. If wave energy dissipation is an important factor along the Oregon coast and the dominant contribution to the DF levels observed at COR is produced nearshore by evanescent pressure excitation spectrum components, then the relative levels of DF microseisms will be correspondingly lower than that expected from the associated wave spectral levels observed at buoy 46050 located  $\sim 38$  km offshore.

[39] The secondary importance of variable wind speed,  $W_s$ , and wind direction,  $W_d$ , for providing opposing wave components in near-coastal locations at wave frequencies  $< 0.2$  Hz is demonstrated by comparing the wave climatology and DF levels for the 17–18 March event. Although  $W_d$  is approximately from the east during 18 March 1999,  $W_s$  is too low and the duration is too short to generate significant long-period energy to provide opposing components for near-coastal wave-wave interaction with the incoming long-period swell. The relatively low  $W_s$  of  $< 6$  m/s observed during 18 March 1999 at buoy 46050 is unrelated to the observed wave spectrum peak at 0.07 Hz in Figure 14, confirmed by the lack of correlation with the associated Pierson-Moskowitz wave spectrum model (Figure 2). Since the wave climatology indicates one long-period swell event, opposing wave components that produce the DF peak near 0.13 Hz must come from shore reflection. These observa-

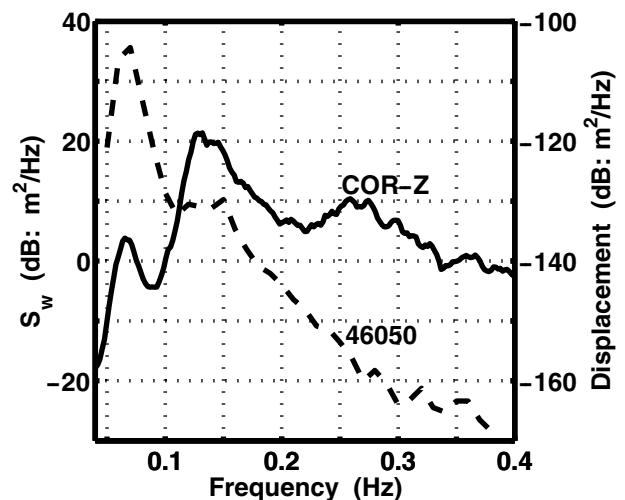


**Figure 14.** Peak of the wave spectrum at 18 March 1999, 0130 UT, for the wave event shown in Figure 12 at the nearshore buoy 46050 (dashed line), with the associated microseism power spectrum at inland station COR (solid line) during the same time period.

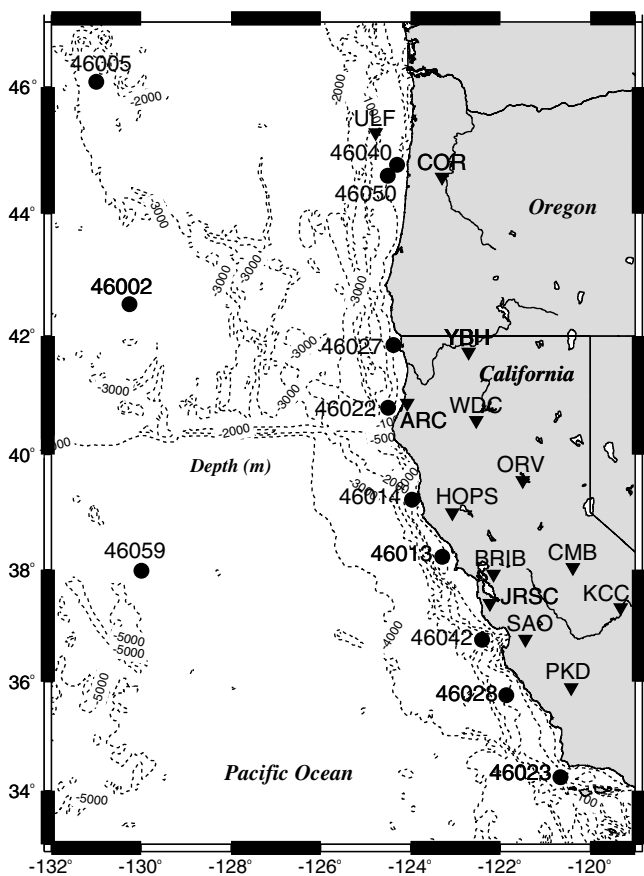


**Figure 15.** Locations of NOAA coastal buoys (solid circles) and the seismometers sites (solid triangles). Bathymetric contours are in meters below sea level, with the shallowest contour at 100 m.

tions suggest that changes in  $W_d$  and elevated  $W_s$  are not as important as nearshore coastal interaction for providing opposing wave components for near-coastal DF microseism generation.

#### 4. Temporal and Spatial Variation for an Extreme Event

[40] Since microseism energy on land propagates as Rayleigh waves that do not attenuate rapidly, some microseism energy must arrive from nonlocal generation areas. To characterize the spatial and temporal variation of microseism levels along the West Coast and to estimate the potential magnitude of the nonlocal contribution, the temporal variation in spectral levels at three locations both near the coast and ~100 km inland are compared for an extreme wave event during March 1999 where the wave energy was concentrated along the Oregon coast. The locations for NOAA buoys and land-based seismometer stations are shown in Figure 15.

##### 4.1. Near-Coastal Response

[41] This storm event, unlike those discussed above, increased in intensity as it approached the coast, with  $H_s$  nearly doubling between offshore buoy 46005 and near-

coastal buoy 46050. Figure 16 shows the temporal variation in  $H_s$  at three buoys along the West Coast associated with the arrival of swell from this storm at the Oregon coast near buoy 46050. As the swell propagates southward along the coast, microseisms were continuously generated. The associated wave and nearby near-coastal microseism spectra are shown in Figure 17 (see Figure 15 for locations). The selected seismic stations are approximately the same distance from the coast to make comparisons meaningful.

[42] The wave spectra show relatively distinct arrivals, with the dominant primary and DF microseism levels at COR corresponding closely with buoy 46050. However, while the peak DF energy at both HOPS and PKD is found near the wave spectrum peak at the nearby coastal buoy, microseism energy generated at more northerly coastal locations is clearly arriving prior to the swell. The microseisms generated nonlocally, or telemicroseisms, propagate as Rayleigh waves with the primary microseisms observed near 0.07 Hz attenuating more slowly than the DF microseisms. The spectral pattern at HOPS suggests that DF microseism energy arrives from the Oregon coast near 3 March 1999, 0800 UT. The DF microseisms near the peak of the swell arrival at the Oregon coast at 3 March 1999, 0800 UT, cannot be identified at PKD, and the primary microseisms observed at that time at PKD are clearly unrelated to wave activity at nearby buoy 46028. The buoy and seismometer data show that the DF microseisms observed at PKD on 4 March 1999 result primarily from nearby wave activity and propagate northward to HOPS, where they are observed as a bifurcation in the DF dispersion trend. Note that the gravity wave propagation distance from the Oregon coast to southern California is manifested by a reduction in the slope of the dispersion trends at the buoys and corresponding nearby seismometer locations. The swell and microseism spectral levels for the 18 March 1999 event at coastal Oregon (Figure 12b) closely match those for similar swell amplitudes along the California coast (Figure 17), suggesting that microseism generation

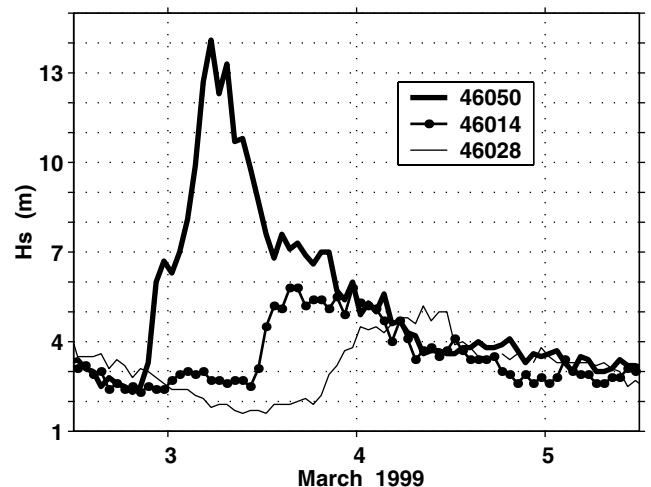


**Figure 16.** Significant wave height,  $H_s$ , at nearshore buoys 46050, 46014, and 46028 during March 1999 showing the concentration of wave energy along the Oregon coast near buoy 46050 (see Figure 15 for locations).

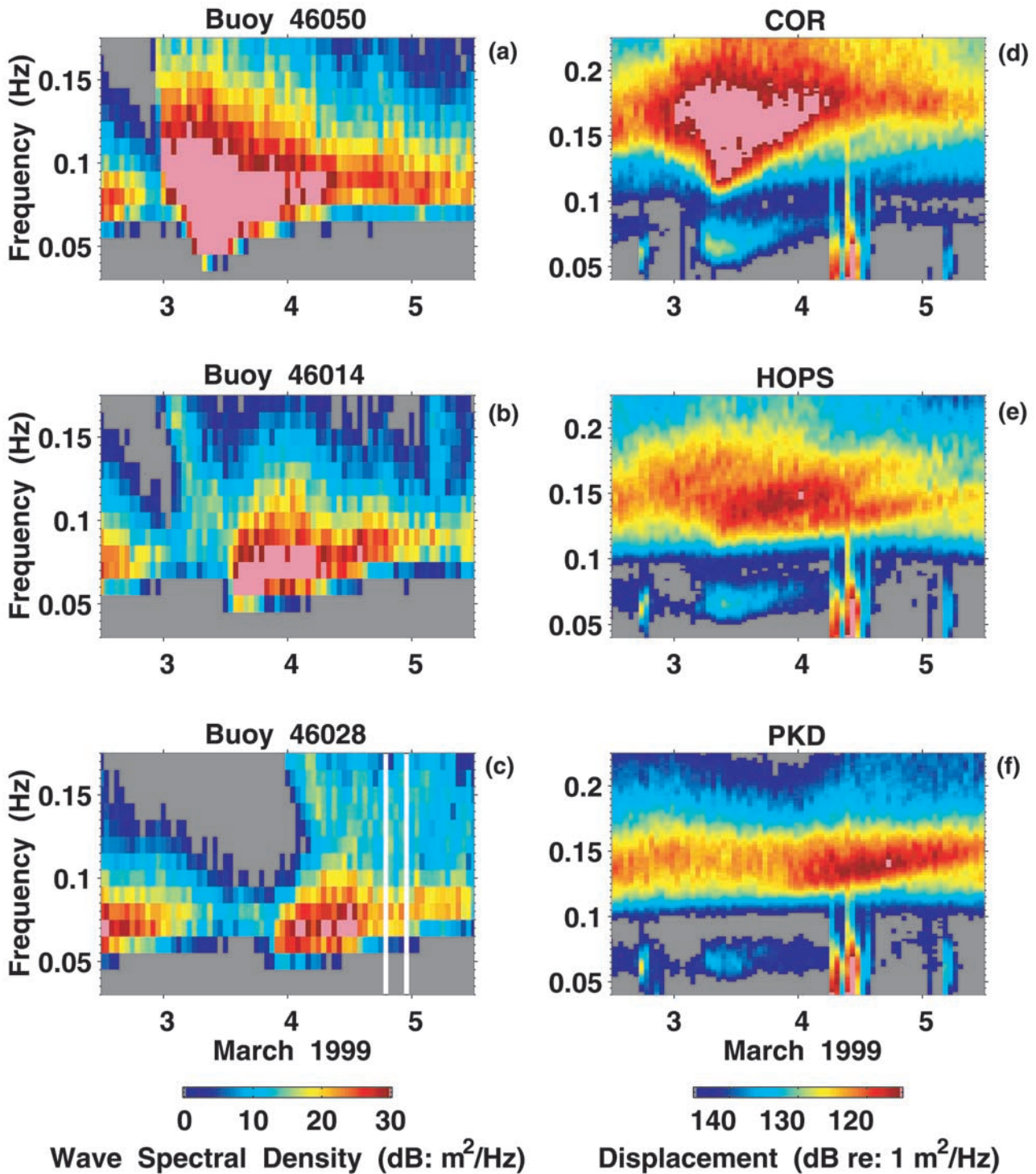


**Figure 17.** Wave and corresponding microseism spectral variation during the southward propagation of gravity waves from an extreme storm event focused along the Oregon coast. Wave spectra at near-coastal buoys (a) 46050, (b) 46014, and (c) 46028. Associated inland near-coastal vertical component microseism power spectra at (d) COR, (e) HOPS, and (f) PKD. Spectral values outside the ranges shown are set equal to their respective bound. See Figure 15 for locations.

does not depend strongly on local coastal bathymetry and geometry.

#### 4.2. Inland Response

[43] Microseism levels farther inland are also dominated by wave activity at the nearest coastline, although the

spectral patterns are less distinct (Figure 18, see Figure 15 for locations). The relative drop in DF microseism levels between Oregon and southern California for the 3 March 1999 event is greater than that of the primary microseisms, consistent with frequency-dependent attenuation. As observed in Figure 17, the highest primary microseism

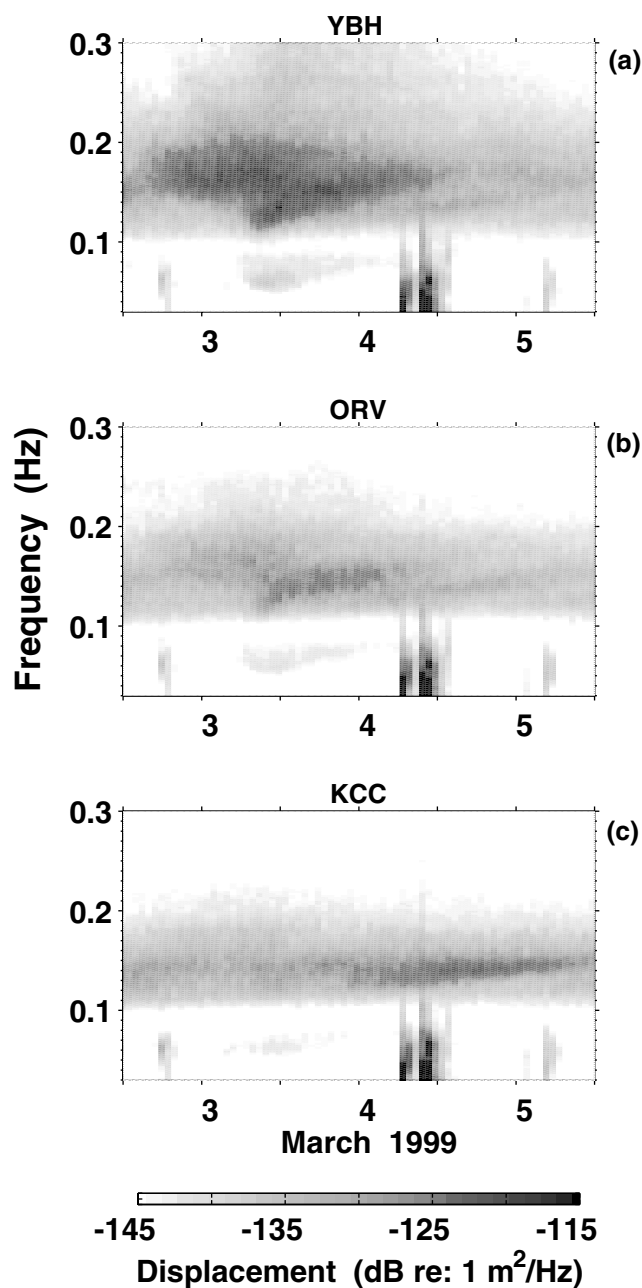


**Figure 18.** Microseism power spectral levels during March 1999 at three inland seismic stations located more than 100 km from the coast (see Figure 15 for locations). Spectral values outside the ranges shown are set equal to their respective bound.

levels are generated when the storm arrives at the Oregon coast and the long-period wave energy is greatest. As swell from this storm propagates down the coast, the long-period components of the wave spectrum decrease in amplitude both from wave front spreading and as a portion of these gravity wave components are refracted into the shore, continuously generating primary and corresponding DF microseisms. The subtle change in the slope of the DF microseism dispersion trends and the shift of the DF maximum to progressively later times indicate that the dominant DF contribution results from wave-wave inter-

actions progressively farther south as the swell propagates along the coast, in agreement with the near-coastal station observations.

#### 4.3. Microseism Attenuation Estimates

[44] Comparison of the spectral levels at buoys 46014 and 46028 (Figure 17) suggests that higher DF microseism levels should be detected at HOPS than at PKD. That this is not the case suggests that either DF generation or DF propagation characteristics (or both) vary along the coast. Estimates of the attenuation characteristics of both primary and DF microseisms can be obtained by comparing spectral levels between seismic stations for the same time period, recognizing that there is some ambiguity in both the propagation path and the source area. The difference in spectral levels (in dB) at the time of the DF microseism spectral peak at the seismic station nearest the coast for a particular associated wave event, scaled by the great circle distance between the stations to account for cylindrical spreading, gives the attenuation,  $\alpha$  (in dB/km). Attenuation estimates (Figure 19) were obtained for the 3–4 March 1999 and the 18 March 1999 wave events (see Figure 15 for station locations). The COR-ORV estimates for both wave events, having distinctly different wave and DF microseism spectral characteristics, give consistent results. In general, high infragravity wave energy decay is observed at frequencies  $<0.05$  Hz between the near-coastal stations closest to the coast and their respective inland pair. Comparison of the attenuation curves in Figure 19 suggests that a zone of distinctly higher attenuation exists within  $\sim 150$  km of the coast between the California/Oregon border and the southern San Francisco Bay region. The similarities of PKD-KCC to SAO-KCC and of JRSC-CMB to BRIB-CMB suggest that the differences in the attenuation curves are not strongly station specific. Note that the attenuation curves both north, COR-ORV, and south, SAO-KCC, of the high-attenuation zone have similar characteristics. The zone of high attenuation explains in part the similar DF microseism spectral levels at HOPS and PKD for relatively higher wave spectral levels at buoy 46014 compared with buoy 46028 levels (see Figure 17).

#### 5. Discussion

[45] Although numerous studies have investigated ocean bottom microseism levels, multiple, colocated, concurrent measurements of wave and microseism spectra in the open ocean away from coastlines and islands have not been made. Consequently, both the variability of microseism source areas for particular storm events and microseism propagation characteristics are not well known. Analyses of microseism particle motion and phase relationships both at the ocean floor [Barstow *et al.*, 1989] and on land [Hau- brich and McCamy, 1969] indicate that microseisms propagate primarily as fundamental mode Rayleigh waves. Since earthquake surface wave energy also propagates as Rayleigh waves through the oceanic basins and then inland, microseisms should behave similarly. However, because the DF microseism source is acoustic, Rayleigh modes at frequencies and wave numbers whose wave functions have much of their energy propagating in the water column will be excited preferentially. Land-based array studies give

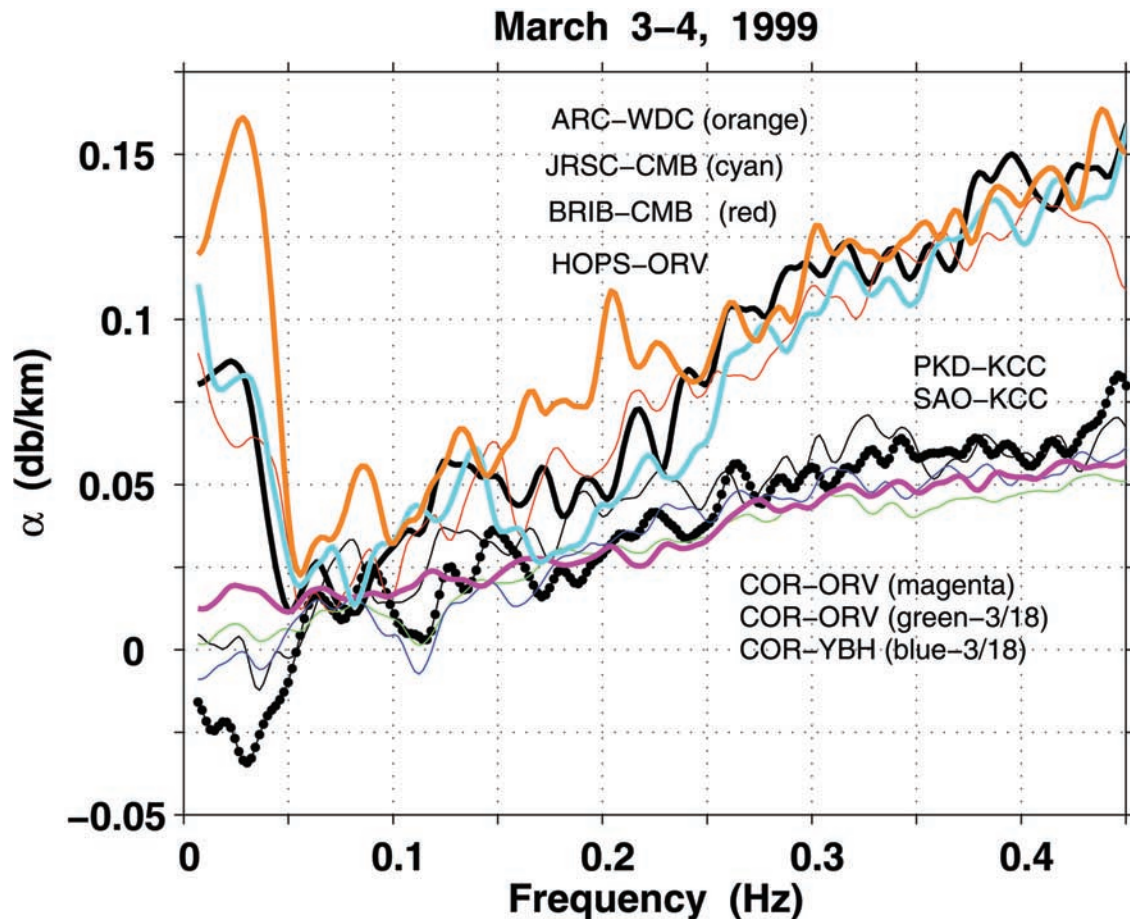


**Figure 19.** Microseism attenuation estimates between near-coastal and inland seismic stations at times of the peak of the DF microseism spectra at the near-coastal station for the 3–4 March 1999 event: HOPS-ORV (solid thick line), PKD-KCC (solid thin line), SAO-KCC (line with solid circles). The other attenuation curves result from the near-coastal/inland station pairs indicated. See Figure 15 for locations. Note that attenuation estimates are also included for COR-ORV and COR-YBH for the 18 March 1999 wave event (see Figure 12).

conflicting results, with *Haubrich and McCamy* [1969] detecting no Rayleigh wave microseism energy arriving from the open ocean, while *Cessaro* [1994] located DF microseism source areas that appear to be generated beneath storms in the deep ocean as well as near the coast. However, Cessaro's open ocean microseism source locations were poorly constrained, possibly resulting from the arrays used in triangulation pointing to different near-coastal locations closer to each respective array and not to the same open ocean locations. The data presented above imply that wave-wave interactions in the open ocean generally do not excite Rayleigh waves that reach near-coastal locations.

[46] The apparent absence of DF microseisms propagating from the region near buoy 46005 during the ULF/VLF experiment and during March 1999 suggests that (1) the opposing wave field is small compared to near-coastal shore-reflected levels so that the microseism levels generated in the open ocean are relatively low, (2) microseism dissipation is high as a result of scattering into Stoneley waves [Schreiner and Dorman, 1990], (3) propagation from deep to shallow water is significantly inhibited by the nature of the changing waveguide [Webb, 1992], (4) refraction of Rayleigh wave modes propagating toward the shore sig-

nificantly reduces the amount of microseism energy reaching near-coastal locations [Hasselmann, 1963], (5) only a small fraction of the downward propagating DF excitation spectrum forces horizontally propagating Rayleigh modes in the open ocean, or, most likely, (6) some combination of the five. These factors, together with the variability of the opposing wave spectrum, cause the magnitude of microseism energy that propagates inland from the open ocean to be uncertain.

### 5.1. Differences Between Near-Coastal DF Levels

[47] Modes generated in deep water that are primarily acoustic will be cut off because of the changing properties of the waveguide as the water depth decreases approaching the coast [Webb, 1992]. Consequently, the near-coastal microseism pressure spectrum at ULF results primarily from local forcing, with any nonoverhead contribution to the bottom pressure spectrum augmented by propagating Rayleigh wave energy from potentially distant locations and also interface wave energy generated nearby [Schmidt and Kuperman, 1988]. With full waveform modeling, Schmidt and Kuperman showed that interface wave energy provides the dominant contribution to the microseism spectrum in

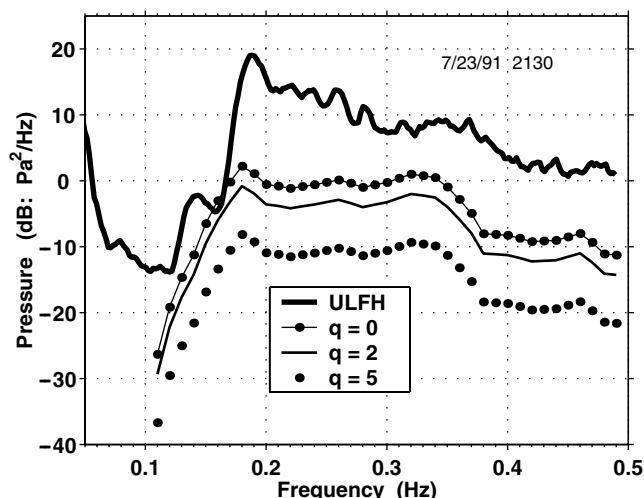


**Figure 20.** Ocean bottom pressure power spectral estimates at ULF-P during 23 July 1991 (thick line) with predicted bottom pressure for beam parameter  $q = 0, 2,$  and  $5$ .

shallow water. Because the ocean bottom is in the near field at ULF (600 m depth), significant microseism excitation can result from evanescent (see Figure 3) as well as acoustic pressure components given by equation (3).

[48] The partition between Rayleigh/Stoneley/Scholte wave energy is strongly dependent on the sediment thickness [Jensen and Schmidt, 1986]. Nearby seismic reflection profiles indicate localized sediment depths of a kilometer or more, with thicker semiconsolidated sediment deposits of <50 km seaward of ULF [Trehu et al., 1995]. Thus the local sediment structure can potentially support interface waves. The amount of interface wave DF energy observed at ULF depends in part on the propagation characteristics of interface waves from generation areas in both nearby seaward and shallower water locations nearer the shore. However, because it is doubtful that the sediment structure and sediment characteristics along the Oregon coast will support low-frequency, low phase velocity Scholte waves and because Scholte waves attenuate rapidly [Jensen and Schmidt, 1986], interface wave energy at ULF is most likely dominated by higher phase velocity Rayleigh/Stoneley waves that can propagate more efficiently along deeper boundaries [Schmidt, 1983].

[49] The similarity in spectral levels for surface wave arrivals from the 20 July 1991 Aleutian earthquake (discussed above) indicate that microseism levels due to Rayleigh wave energy at ULF and COR should be comparable in the [0.04,0.15] Hz band. Since interface wave characteristics are linked to the ocean bottom sediment properties and have a strong seismoacoustic component, they are not expected to propagate well inland. Therefore microseism levels at COR must result mostly from propagating Rayleigh wave energy that should have similar levels at both ULF and COR. Thus the differences in spectral levels between ULF and COR (see Figures 6 and 8) result primarily from seismoacoustic energy that is generated nearby and is observed at ULF but not at COR. These observations indicate that only a relatively small percentage of microseism energy in the form of interface waves observed at the ocean bottom in near-coastal regions propagates inland.

[50] The contribution of interface wave and Rayleigh wave energy to the DF microseism levels at ULF can be estimated by comparing the ocean bottom pressure at ULF-P with the high phase velocity nonresonant pressure excitation spectrum (equation (3)) estimated from wave spectrum measurements. Figure 20 shows one realization of the pressure spectral levels at ULF-P during the boreal swell arrival on 23 July 1991, with the predicted bottom pressure computed for wave spectral data from buoy 46040 (see Figure 8) during the same time period using equation (6) for isotropic,  $q = 0$ , and more narrow-beam wave field directional dependencies. The difference between ULF-P and the prediction for  $q = 0$  represents the lower bound for the seismoacoustic contribution to DF levels at ULF. Near the dominant DF microseism peak at  $\sim 0.19$  Hz (Figure 20) the difference between the measured and predicted pressure levels is  $\sim 20$ – $30$  dB, in general agreement with the increase from propagation effects demonstrated by Schmidt and Kuperman [1988] and consistent with the differences in DF levels observed between ULF-Z and COR-Z in Figure 8.

**5.2. Signal Amplitude Implications**

[51] Amplitude comparisons between ocean bottom ULF and inland COR spectral levels allow the differentiation between high phase velocity Rayleigh waves and other gravity wave induced signals. Investigation shows that spectral levels for the trend c signals in Figure 11a (Figure 21a, arrows) are higher than those for the shorter-

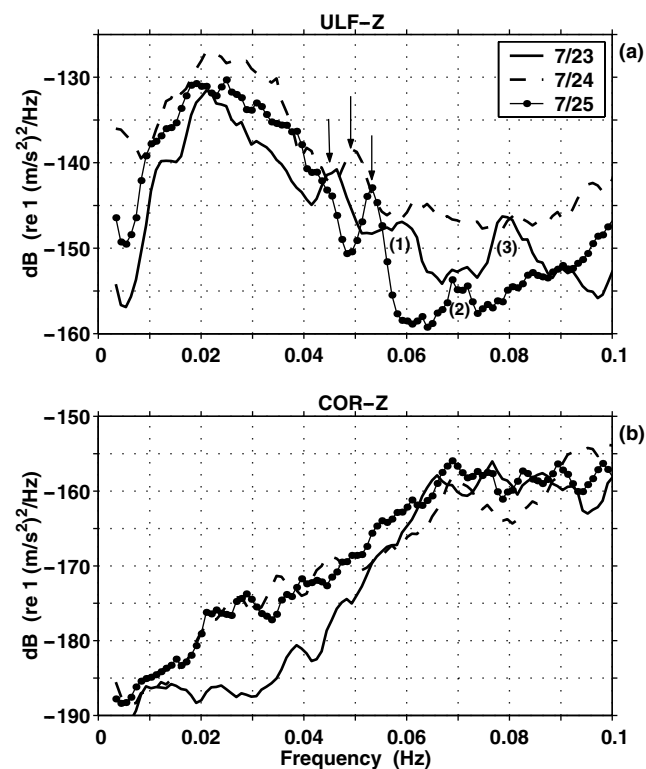


**Figure 21.** Acceleration response power spectral estimates for vertical component seismometers at ocean bottom ULF-Z and inland COR sites at 0000 UT on 23, 24, and 25 July 1991. Arrows indicate spectral peaks associated with the austral swell trend c in Figure 11. Numbers refer to primary microseism peaks discussed in the text.

period boreal event on 23 July (Figure 21a, spectral peak 3). However, associated DF microseisms for trend c are not observed at ULF (Figure 11a), and neither primary nor DF microseisms for these swell arrivals are identifiable at COR (Figure 21b). The ratio of the vertical acceleration to the pressure at the ocean bottom for trend c is on the order of  $10^{-8} \text{ m}^{-1} \text{ s}^{-2} \text{ Pa}^{-1}$ , in the range expected for ocean waves [Crawford *et al.*, 1991]. Inversion of the ocean bottom pressure of  $\sim 18 \text{ Pa}^2 \text{ Hz}^{-1}$  at 0.05 Hz using equation (7) gives a forcing wave height much less than 1 cm, well below the detection range of surface buoys. These factors suggest that trends a, b, and c may result entirely from overhead hydrodynamic forcing and that Rayleigh wave energy may be entirely absent. If these trends resulted partially from microseism energy generated near shore, then they would be observed in horizontal acceleration spectra. However, because the horizontal noise levels from other sources near 0.05 Hz were much higher than the vertical noise levels (see Figure 8), it cannot be determined conclusively that dispersion trends a, b, and c do not contain a seismic component.

[52] Because the detection of trend c signals at ULF indicates that these long-period waves reach shallow water with resulting refraction toward the shore, they should generate primary and DF microseisms detectable at COR. Gravity wave reflection from beaches is most efficient for low-amplitude, long-period swell [Elgar *et al.*, 1994]. However, efficient reflection does not produce the nonlinear effects associated with nearshore shoaling and wave breaking that are necessary to generate high phase velocity primary microseism Rayleigh waves that can propagate inland [Hasselmann, 1963]. Since swell associated with trend c will reflect more efficiently than the shorter-period boreal swell on 23 July, the absence of associated DF microseisms at ULF for trend c indicates that shore reflection of this swell does not produce sufficient opposing components over a large enough interaction zone to generate detectable DF microseisms. This suggests that these extremely low amplitude wave components are either dissipated and/or converted into trapped edge waves [Guza and Thornton, 1982]. The absence of DF microseisms associated with trends a, b, and c also indicates that there was virtually no opposing wave energy at frequencies  $< 0.07$  Hz in the open ocean.

[53] Spectral peak 1 (Figure 21) is associated with the trend b arrival (Figure 11a) and also most likely results primarily from hydrodynamic forcing, while spectral peak 2 results from the shorter-period, higher-amplitude austral arrival that causes the narrowband primary and DF microseisms observed at COR-Z (Figure 6f) near 0.065 and 0.13 Hz, respectively. Note that spectral levels at COR are similar to the levels at ULF at the time of peak 2, suggesting that these phases result almost entirely from Rayleigh waves having about the same offshore/onshore propagation characteristics as the 20 July earthquake (Figures 11a and 11b). The sharp hydrodynamic cutoff (see Figure 5) results in no added pressure signal for these shorter-period waves (and those causing trends d and e, Figure 11a) at 600 m depth.

## 6. Conclusion

[54] The spatial and temporal variation of microseism levels in near-coastal regions is directly related to wave

energy levels at nearby coastlines. The correspondence between the near-coastal ocean bottom and near-coastal inland double-frequency, DF, microseism levels is almost one-to-one. The highest primary microseism levels for a storm event are generally associated with the coastal location where the storm swell initially reaches the shore, potentially at relatively long distances from seismic stations. In contrast, DF levels at near-coastal seismometers are dominated by wave-wave interactions at the nearest coastlines. During a low sea state wave climate, near-coastal ocean bottom microseism levels are generally  $\sim 20$  dB higher than those on land nearby. This difference is attributed primarily to seismoacoustic DF energy generated both locally and in shallower water nearer the shore. Comparison of offshore and nearshore wave spectral variation with near-coastal microseism levels indicates that little DF microseism energy from the open ocean reaches the coast. Whether this results primarily from microseism propagation characteristics while traveling from offshore to nearshore areas or the lack of energy in opposing wave components causing relatively low DF microseism generation in the open ocean is unknown.

[55] **Acknowledgments.** The California Department of Boating and Waterways supported this research as part of their program to improve boating facilities, access, safety, and education. We thank Spahr Webb, Charles Cox, and Reinhard Flick for helpful discussions and LeRoy Dorman and Bob Guza at SIO for reviewing the manuscript. Steve Pendlebury of the Bureau of Meteorology, Melbourne, Australia, provided weather charts for the South Pacific and Southern Oceans, and Scott Jenkins of CCS/SIO assisted in their interpretation. We thank Alan Rohay of Battelle PNL for support of the initial analyses of these data. Thoughtful reviews by George Helffrich, Barbara Romanowicz, and an anonymous referee helped to focus the manuscript.

## References

- Barstow, N., G. H. Sutton, and J. A. Carter, Particle motion and pressure relationships of ocean bottom noise: 3900 m depth; 0.003 to 5 Hz, *Geophys. Res. Lett.*, **16**, 1185–1188, 1989.
- Bouws, E., and G. J. Komen, On the balance between growth and dissipation in an extreme depth-limited wind-sea in the southern North Sea, *Bull. Am. Meteorol. Soc.*, **13**, 1653–1658, 1983.
- Bretschneider, C. L., Wave variability and wave spectra for wind-generated gravity waves, *Tech. Memo. 118*, 192 pp., Beach Erosion Board, Washington, D. C., 1959.
- Bromirski, P. D., and F. K. Duennebieer, Seismo-acoustic signals and noise in the near-shore environment, *SOEST Rep. 95-03*, 120 pp., Univ. of Hawaii, Honolulu, 1995.
- Bromirski, P. D., R. E. Flick, and N. Graham, Ocean wave height determined from inland seismometer data: Implications for investigating wave climate changes in the NE Pacific, *J. Geophys. Res.*, **104**, 20,753–20,766, 1999.
- Cessaro, R. K., Sources of primary and secondary microseisms, *Bull. Seismol. Soc. Am.*, **84**, 142–156, 1994.
- Cox, C. S., and D. C. Jacobs, Cartesian diver observations of double frequency pressure fluctuations in the upper levels of the ocean, *Geophys. Res. Lett.*, **16**, 807–810, 1989.
- Crawford, W. C., S. C. Webb, and J. A. Hildebrand, Seafloor compliance observed by long-period pressure and displacement measurements, *J. Geophys. Res.*, **96**, 16,151–16,160, 1991.
- Dorman, L. M., A. E. Schreiner, and L. D. Bibee, The effects of shear velocity structure on seafloor noise, in *Shear Waves in Marine Sediments*, edited by J. M. Hovem *et al.*, pp. 239–245, Kluwer Acad., Norwell, Mass., 1991.
- Elgar, S., T. H. C. Herbers, and R. T. Guza, Reflection of ocean surface gravity waves from a natural beach, *J. Phys. Oceanogr.*, **24**, 1503–1511, 1994.
- Ewing, W. M., W. S. Jardetsky, and F. Press, *Elastic Waves in Layered Media*, 380 pp., McGraw-Hill, New York, 1957.
- Forristall, G. Z., and A. M. Reece, Measurements of wave attenuation due to a soft bottom: The SWAMP experiment, *J. Geophys. Res.*, **90**, 3367–3380, 1985.

- Guza, R. T., and E. B. Thornton, Swash oscillations on a natural beach, *J. Geophys. Res.*, *87*, 482–491, 1982.
- Hasselmann, K., A statistical analysis of the generation of microseisms, *Rev. Geophys.*, *1*, 177–210, 1963.
- Haubrich, R. A., and K. McCamy, Microseisms: Coastal and pelagic sources, *Rev. Geophys.*, *7*, 539–571, 1969.
- Herbers, T. H. C., and R. T. Guza, Wind-wave nonlinearity observed at the seafloor, part I, Forced-wave energy, *J. Phys. Oceanogr.*, *21*, 1740–1761, 1991.
- Hughes, B., Estimates of underwater sound (and infrasound) produced by nonlinearly interacting ocean waves, *J. Acoust. Soc. Am.*, *60*, 1032–1039, 1976.
- Jensen, F. B., and H. Schmidt, Shear properties of ocean sediments determined from numerical modeling of Scholte wave data, in *Ocean Seismo-Acoustics*, edited by T. Akal and J. M. Berkson, pp. 683–692, Plenum, New York, 1986.
- Kibblewhite, A. C., and K. C. Ewans, Wave-wave interactions, microseisms, and infrasonic ambient noise in the ocean, *J. Acoust. Soc. Am.*, *78*, 981–994, 1985.
- Kibblewhite, A. C., and C. Y. Wu, The theoretical description of wave-wave interactions as a noise source in the ocean, *J. Acoust. Soc. Am.*, *89*, 2241–2252, 1991.
- Kuperman, W. A., and H. Schmidt, Self-consistent perturbation approach to rough surface scattering in elastic media, *J. Acoust. Soc. Am.*, *86*, 1511–1522, 1989.
- Longuet-Higgins, M. S., A theory of the origin of microseisms, *Philos. Trans. R. Soc. London, Ser. A*, *243*, 1–35, 1950.
- Munk, W. H., G. R. Miller, F. E. Snodgrass, and N. F. Barber, Directional recording of swell from distant storms, *Philos. Trans. R. Soc. London, Ser. A*, *259*, 505–584, 1963.
- Orcutt, J. A., C. S. Cox, A. C. Kibblewhite, W. A. Kuperman, and H. Schmidt, Observations and causes of ocean and seafloor noise at ultra-low frequencies, in *Natural Physical Sources of Underwater Sound*, edited by B. Kerman, pp. 203–232, Kluwer Acad., Norwell, Mass., 1993.
- Pierson, W. J., Jr., and L. Moskowitz, A proposed spectral form for fully developed wind seas based on the similarity theory of S. A. Kitaigorodskii, *J. Geophys. Res.*, *69*, 5181–5190, 1964.
- Romanowicz, B., D. Neuhauser, B. Bogaert, and D. Oppenheimer, Accessing Northern California Earthquake Data Center via Internet, *Eos Trans. AGU*, *75*, 257, 259, 260, 1994.
- Schmidt, H., Excitation and propagation of interface waves in a stratified sea-bed, *Acoustics and the Sea-Bed*, edited by N. G. Pace, pp. 327–334, Bath Univ. Press, Bath, England, 1983.
- Schmidt, H., and W. A. Kuperman, Estimation of surface noise source level from low-frequency seismoacoustic ambient noise measurements, *J. Acoust. Soc. Am.*, *84*, 2153–2162, 1988.
- Schreiner, A. E., and L. M. Dorman, Coherence lengths of seafloor noise: Effect of ocean bottom structure, *J. Acoust. Soc. Am.*, *88*, 1503–1514, 1990.
- Steele, K. E., J. C. Lau, and Y. L. Hsu, Theory and application of calibration techniques for an NDBC directional wave measurements buoy, *IEEE J. Oceanic Eng.*, *10*, 382–396, 1985.
- Trehu, A. M., G. Lin, E. Maxwell, and C. Goldfinger, A seismic reflection profile across the Cascadia subduction zone offshore central Oregon: New constraints on methane distribution and crustal structure, *J. Geophys. Res.*, *100*, 15,101–15,116, 1995.
- Webb, S. C., The equilibrium oceanic microseism spectrum, *J. Acoust. Soc. Am.*, *92*, 2141–2158, 1992.
- Webb, S. C., Broad-band seismology and noise under the ocean, *Rev. Geophys.*, *36*, 105–142, 1998.
- Webb, S. C., and C. S. Cox, Observations and modeling of sea floor microseisms, *J. Geophys. Res.*, *91*, 7343–7358, 1986.
- Welch, P. D., The use of the fast Fourier transform for the estimation of power spectra: A method based on time averaging over short, modified periodograms, *IEEE Trans. Audio Electroacoust.*, *AU-15*, 70–73, 1967.

---

P. D. Bromirski, Integrative Oceanography Division Scripps Institution of Oceanography, University of California, 8650 Discovery Way, La Jolla, CA 92093-0209, USA. (pbromirski@ucsd.edu)

F. K. Duennebieer, Department of Geology and Geophysics, University of Hawaii, Honolulu, HI 96822, USA. (fred@akule.soest.hawaii.edu)